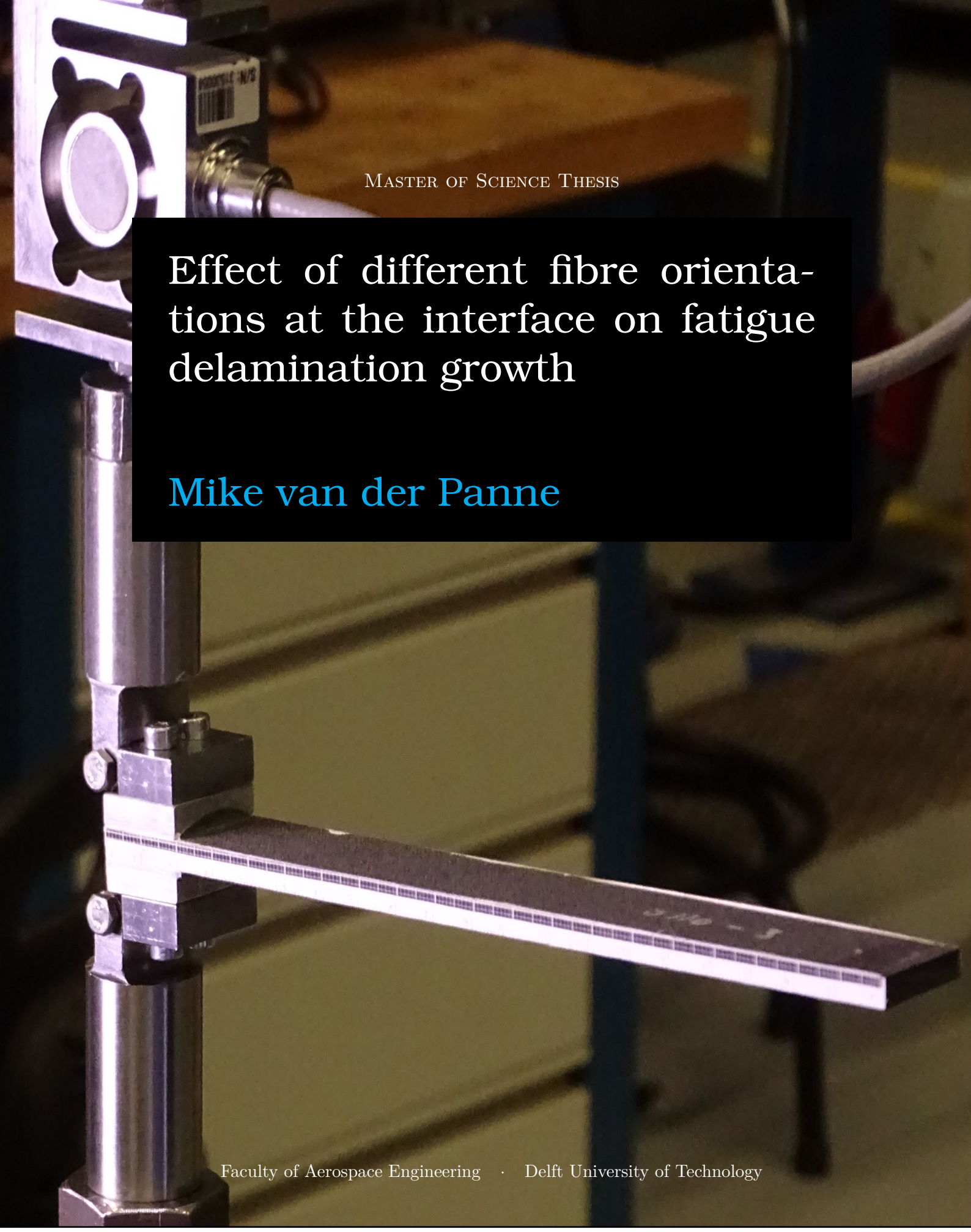

Master of Science Thesis

Effect of different fibre orientations at the interface on fatigue delamination growth

Mike van der Panne

Faculty of Aerospace Engineering · Delft University of Technology

TU Delft Delft University of Technology

Effect of different fibre orientations at the interface on fatigue delamination growth

Master of Science Thesis

For obtaining the degree of Master of Science in Aerospace Engineering
at Delft University of Technology

Mike van der Panne

13 April 2022

Faculty of Aerospace Engineering · Delft University of Technology

Delft University of Technology
Faculty of Aerospace Engineering
Department of Aerospace Structures and Materials

GRADUATION COMMITTEE

Dated: 13 April 2022

Chair holder:

Dr.ir. R.C. Alderliesten

Committee members:

Dr.ir. J.A. Pascoe

Dr. B. Giovanardi

Dr. M. Mega

Preface

This document is the results of my Master science graduation project on the subject of mode I fatigue delamination growth. It was a period which started with lab work, consisting of manufacturing and testing. After this, a closer look at the many pictures was taken. This was the beginning of the analysis period and eventually the writing of this report. This process and the results are described in this report.

This master thesis report would not have been possible without the support of several people. First, the DASML technicians for giving me with their knowledge during the manufacturing of the laminates. With special attention to Fred Bosch and Dave Ruijtenbeek for their help on respectively the autoclave and the test bench. Second, Lars Smit with whom I worked together in the laboratory laminating. Third, Jort Roelofs and Apura Venkatesh for their feedback on my report. Special thanks go out to my friends, parents and other family who supported me throughout this research. Last, most of all I would like to thank my supervisor John-Alan Pascoe for his support, guidance, feedback and discussions.

Yours sincerely,

Mike van der Panne

Abstract

Composite materials have multiple failure modes. Most of these failure modes are dedicated to the different layers, e.g., delamination. Unfortunately, these damages can occur internally, causing it to be invisible to the naked eye. A better understanding of how this happens and what causes it, is required to ensure safety. Therefore, for this research, delamination is the most interesting failure mode. Previous researches have primarily been focusing on quasi-statically loaded UD specimen. However, since a layup in a structural part of an aircraft consists of multiple layers with different fibre orientations, it is not guaranteed that a delamination will occur between two 0° plies. Furthermore, an aircraft is designed to be in service for decades and consequently is loaded thousands of times. A structure which is subjected to a cyclic loading will behave differently than one to a quasi-static loading. Hence, in aviation industries, tests with cyclically loaded specimens are more relevant.

This research project focused on fatigue delamination crack growth of multi-directional interfaces. In order to generate mode I delamination, DCB specimens were manufactured and tested. Fatigue experiments were conducted to see the influence of the interface angle as well as that of the orientation of the interface angle. To cover most relevant delamination planes, tests with the following interface were conducted: $0°//0°$, $45°//45°$, $90°//90°$, $0°//45°$, $0°//90°$, $45°//-45°$ and $30°//-60°$. Furthermore, the crack fronts were monitored by means of C-scans and the fracture surfaces were examined.

It was found that for all different interface orientations, fibres bridged. This was demonstrated with an increased delamination resistance for a longer crack. The nature of these bridging fibres, however, differed. Fibre bridging regarding to nesting showed a less significant increase in fracture resistance than bridging fibres due to oscillatory crack propagation behaviour. Furthermore, the different interfaces showed various crack fronts. The crack front tends to propagate towards the direction of the fibres of either of the fibre orientations around the interface.

Table of Contents

Nomenclature

Symbol/Abbreviation	Meaning	Unit
α	Angle	$^\circ$
γ_p	Plastic energy dissipation per unit area of crack growth	J/m^2
γ_s	Specific surface energy for atomic bond breakage	J/m^2
δ	Displacement	m
ν	Poisson's ratio	-
σ	Stress	N/m^2
a	Crack length	m
a_0	Initial crack length	m
b	Specimen width	m
B_t	Stiffness ratio	-
C	Compliance	m/N
C	Fitting parameter	-
DASML	Delft Aerospace Structures and Materials Laboratory	-
D_c	Stiffness ratio	-
DCB	Double cantilever beam	-
D_{ij}	Bending stiffness components	Nm
E	Young's modulus	N/m^2
FRP	Fibre reinforced polymers	-
G	Strain energy release rate	J/m^2
h	Specimen thickness	m
K	Stress intensity factor	$N/m^{1.5}$
m	Slope of the plot of a/h vs $C^{1/3}$	$(N/m)^{1/3}$
MCC	Modified compliance calibration	-
MD	Multi-directional	-
N	Number of cycles	-
n	Fitting parameter	-
P	Load	N
R	Ratio	-
SERR	Strain energy release rate	J/m^2
SIF	Stress intensity factor	$N/m^{1.5}$
U	Energy	J
UD	Uni-directional	-
U_e	Release energy	J
U_s	Surface energy	J

Chapter 1

Introduction

1.1 Background

The use of composite materials is significantly increasing in the aviation industry [1]. Multiple structures contain fibre reinforced polymers (FRP) instead of their metallic predecessors [2]. This can be explained by their superior material properties. The major benefit of using FRP instead of metals is the high(er) specific strength and stiffness. This results in improved aircraft performance as it can be designed lighter [3]. Furthermore, composite materials do not experience corrosion and have better fatigue resistance than their metallic counterparts [4] [5]. To make a long story short, the aerospace industry can benefit heavily from the use of composite materials.

However, composite materials also have their flaws. The knowledge and understanding of these materials leave room for improvement [6]. For that reason, the usage of FRP in primary structures was withheld. The development of using composites started in the 20th century, whereas metals have been used for centuries. Although metals are more familiar, the promising prospects of composite materials have already contributed to major composite incorporated aircraft parts, e.g., wings and fuselage [2]. Another reason behind the prevention of using composite materials is the lack of visual damage. For these structures, it is harder to see whether they are damaged internally [7]. Where metals, such as aluminium, show dents on the outside, a composite could have an internal crack without showing it.

When it comes to failure, composite materials have an increased number of failure modes compared to metals. Some failure modes are similar, e.g., tensile and compressive failure, while others are unique to composite materials. Most of these additional failure mechanisms are dedicated to the different layers, e.g., delamination. Unfortunately, this damage can occur internally causing it to be invisible to the naked eye. Therefore, a better understanding of how this happens and what causes it is required.

Delamination on its own has different origins. The mechanisms that play an important role are: impact, peeling and compression [8]. These all lead to a local increase in interlaminar stresses. If that exceeds a certain threshold, a crack could start to grow. In this document, the

terms delamination and crack growth are used for the same phenomenon, i.e., crack growth. The other delamination mechanisms are not included in this research.

The research for delamination in composite materials has already been studied for several years, as can be seen in Chapter 2. However, most of the research focuses on quasi-statically loaded 0° unidirectional (UD) layers. In reality, there is no guarantee that a delamination will occur between those plies, and what would happen if the structure is in service for multiple load cycles. This research aims for a better understanding of the influence of the direction of the fibres at the interface under fatigue.

1.2 Thesis Objective

The objective of this thesis is to achieve a better understanding of the effect of having different fibre orientations at the delamination interface when cyclic loaded by means of experiments and with examining the fracture surfaces. In this report, the necessary steps of this research project are presented to answer the research question: "What is the influence of the fibre orientation at the interface on delamination growth rate under cyclic loading?".

1.3 Structure of the Report

First, an overview of the research that has already been done is given in Chapter 2. From this review, a research question was drawn, see Chapter 3. This chapter includes the hypothesis for the question. To answer the research question, a test plan is presented in Chapter 4, and the methodology of the manufacturing, experimental and analysis processes is described in Chapter 5. The results of the experiments are shown in Chapter 6. In Chapter 7, the results are discussed and compared with previous literature. This will be concluded with recommendations in Chapter 8.

Chapter 2

Literature Review

In this chapter, an overview of the literature study on delamination growth performed earlier is given. This study is separated into four topics. First, strain energy release rate is introduced in section 2.1. In section 2.2, the effects of cyclic loading are described. After this, section 2.3 covers delamination growth of multi-directional layups. Then, the presence of fibre bridging and their effect on the strain energy release rate is explained in section 2.4. At last, research in the field of the combination of both multi-directional and cyclic loading is discussed.

2.1 Strain Energy Release Rate

Nowadays, methods trying to understand crack growth are based on the fundamentals of Griffith [9]. This is based on the association of an energy change with structural failure, in this case, delamination. In order to grow a crack, energy is required. In short, when a crack growths new surfaces are formed. The formation of these new surface areas requires energy. Consequently, crack growth requires energy.

On the other hand, crack growth does not only require energy. Stored elastic energy is released in case a crack is enlarged [10]. In order to know whether a crack will grow depends on the magnitude of the energy level, i.e. which of the values is higher, the surface energy (U_s) or the released energy (U_e). Griffith's energy criterion to have crack growth is: $U_e \geq U_s$ when $dU/da = 0$, in which U is the total energy and a the crack length [10]. Knowing this it can be derived that the strain energy release rate (SERR) for brittle solid materials is expressed as:

$$G_I = 2\gamma_s = \frac{\pi a \sigma^2}{E'} \tag{2.1}$$

With,

$$E' = E \text{ for plane stress} \tag{2.2}$$

and,

$$E' = \frac{E}{1-\nu^2} \text{ for plain strain} \tag{2.3}$$

where γ_s is the specific surface energy for atomic bond breakage, σ is the applied stress, E is the Young's modulus, and ν is the Poisson's ratio. In order to see whether there is unstable fracture and thus crack growth, the SERR should be higher than a critical value, i.e., the crack will grow when $G_I \geq G_{Ic}$. For a UD FRP under quasi-static loading, the critical SERR is determined according to the ASTM D5528 test standard [11].

Griffith did experiments with glass [9]. This has its benefit that there was only one mechanism of energy consumption when new surfaces are created [12], whereas most materials also have a plastic region around the crack tip [10]. Consequently, an additional term needs to be added to Equation 2.1. Besides the term for a perfectly brittle breakage, a term for the plasticity of the material is incorporated [13] [14]:

$$G_I = 2(\gamma_s + \gamma_p) \tag{2.4}$$

where γ_p is the energy dissipation due to plastic deformation around the crack tip. This becomes important for materials such as metals which dissipate less energy with atomic bond breakage than with plastic deformation near a crack tip. In fact, for metals this is significantly larger, i.e., $\gamma_p \gg \gamma_s$ [10].

When rearranging Equation 2.1, the stress intensity factor (SIF) for an infinite plate can be separated [15].

$$\sqrt{G_I E'} = \sigma\sqrt{\pi a} \tag{2.5}$$

$$K_I = \sigma\sqrt{\pi a} \tag{2.6}$$

The SIF (K_I) is the term to describe the fracture toughness of the material [16]. It can be seen that it has some similarities with SERR, see Equation 2.5. This relation between SERR and SIF is also demonstrated by Irwin through combining Equation 2.5 and Equation 2.6 [17] [18].

$$G_I = \frac{{K_I}^2}{E'} \tag{2.7}$$

2.2 Fatigue Crack Growth

In the aviation industry, most parts are cyclically loaded. Accordingly, the expression correlating to the fatigue crack growth should incorporate cyclic loading. In subsection 2.2.1, it is explained how to determine the SERR in fatigue. The introduction of additional variables due to cyclic loading is described in subsection 2.2.2.

2.2.1 Paris Relation

The fundamentals of fracture mechanics for cyclic loading are based on the framework of Paris et al. [19] [20] [21]. Since the magnitude of the applied stress fluctuates, the crack growth rate should be related to the alternating SIF of the crack tip [22]. This led to the basic formula describing the delamination growth per cycle [19] [20] [21]:

$$\frac{da}{dN} = C(\Delta K)^n \tag{2.8}$$

where N is the number of cycles, and C and n are fitting parameters. As described in section 2.1, SIF is more commonly used for metals. The equivalence of the SIF and the SERR makes it, therefore, feasible to modify Equation 2.8 in terms of SERR. However, the value of the SERR differs during each cycle. This gives the option to use either G_{max} or ΔG. A preference between the two differs per research/person as both methods are shown to be successful [23]. Accordingly, the delamination growth per cycle can be generally expressed as:

$$\frac{da}{dN} = Cf(G)^n \tag{2.9}$$

in which, $f(G)$ could represent G_{max} or ΔG. When using ΔG, one should be aware that the correct expression for ΔG according to the equivalent of ΔK, is rather [24] [25]:

$$\Delta\sqrt{G} = (\sqrt{G_{max}} - \sqrt{G_{min}})^2 \tag{2.10}$$

instead of

$$\Delta G = G_{max} - G_{min} \tag{2.11}$$

2.2.2 Additional Fatigue Parameters

The introduction of fatigue testing brings additional variables compared to quasi-static testing, see section 2.1. First, the frequency of the cycles plays an important role. In order to reduce the duration of the test, a higher frequency is wanted. On the other hand, the local temperature of the specimen could increase significantly by increasing the frequency [26] [27] [28]. This could affect the results. In fact, the temperature plays an important role in how the composite material behaves [29]. For that reason, a limitation of the frequency is given in the ASTM D6115 test standard [30].

Second, fatigue loading has peaks and valleys in its cycle. The load will not be increased until breakage, but it fluctuates between certain loadings or displacements. Either the maximum and minimum loadings or displacements, are kept constant during the test. One way to express this is by means of a ratio (R). For example, a test performed at a load ratio of 0.1 is defined as:

$$R = \frac{P_{min}}{P_{max}} = 0.1 \tag{2.12}$$

As can be seen in Equation 2.9,the equation for the fatigue delamination growth does not include any ratio. Nevertheless, a different ratio causes different results [31]. Thus, some researchers try to incorporate this ratio in a SERR expression instead of trying to understand the physics behind it [32]. Furthermore, Wilkins et al. noted that the SERR ratio $\frac{G_{min}}{G_{max}}$ is proportional to R^2 [33].

2.3 Multi-Directional Layup

With the introduction of multi-directional (MD) plies the whole laminate behaves differently. In order to limit unwanted behaviour the layup should be stacked in a certain order. This is done to reduce (some) B- and D-matrix values, see subsection 2.3.1. The introduction of MD plies causes additional modes, i.e., mode II and mode III, see subsection 2.3.2.

2.3.1 B- and D-matrix values

A specimen with a multi-directional layup is, as its name already predicts, not equal to an UD specimen, which has all the fibres directed in the same direction. The fibres in the non-zero direction could contribute to unwanted behaviour. Especially an asymmetric layup, this will generate a coupling, i.e., the B and D terms of the ABD matrix are non-zero. This implies that in the test for mode I (ASTM D5528 [11]), an asymmetric specimen also faces mode II. As an asymmetric layup is inevitable when testing a non-zero interface angle, these phenomena have to be limited.

During the design, the coupling should be reduced as much as possible. When possible, the laminate should be symmetric in order to obtain a zero B matrix. As described before, an asymmetric layup will have a non-zero B matrix. Thus, one should come up with a design to reduce them.

Similarly, it is advised to get the stiffness ratio values as close to zero as possible [34] [35] [36]. These stiffness ratio values, D_c and B_t, have a direct influence on the crack front. It affects both the skewness and the curvature of the G distribution, see Figure 2.1. In Table 2.1, the corresponding layups are given. Note: In Figure 2.1, the letter "s" is used instead of B_t, however, the same is meant.

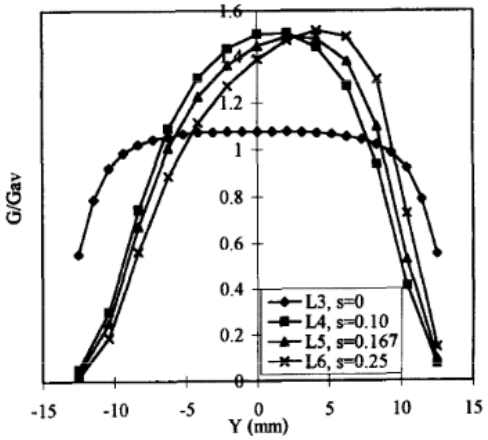

Figure 2.1: G distribution along the crack front for several layups [36]

Table 2.1: Several layups with corresponding B_t value [36]

Specimen	Layup sequence	B_t
L3	$[0]_{12}$	0
L4	$[\pm 45]_5 s$	0.10
L5	$[\pm 45]_3 s$	0.167
L6	$[\pm 45]_2 s$	0.250

The higher the values of D_c and B_t, the lesser the G distribution looks like that of an UD laminate. This can also be seen in how these values are expressed [34] [36]:

$$D_c = \frac{D_{12}^2}{D_{11} D_{22}} \tag{2.13}$$

$$B_t = \frac{D_{16}}{D_{11}} \tag{2.14}$$

where D_{ij} are the bending stiffness components known from classical laminate theory, in which, the longitudinal, transverse and shear directions are indicated respectively with the indices: i,j = 1,2,6.

It can be seen that for a layup with solely 0° layers, B_t will be zero. Additionally, certain combinations of layers cause the D_{16} value to be zero and thus B_t as well, e.g., anti-symmetric layups. A non-zero B_t will have a skew distribution of the SERR across the width. Although, it is theoretically possible to obtain a zero B_t value, a different layup is a better solution to the requirements in many cases. In order to cope with that, it is suggested to limit B_t to a value of 0.1 or lower [35].

Contrary to B_t, D_c will be non-zero even for an UD specimen [34]. Nevertheless, these values needs to be limited, since the effect of finite width will play a larger role with a higher value. The larger the value of D_c, the larger the SERR variation across the specimen width [35]. Hence, Davidson et al. suggest a 'limiting value' of $D_c = 0.25$ for the test specimen [34]. Although these values will differ over various applications, i.e., lesser/stricter tolerances. For now, these values will be taken as guideline.

2.3.2 Mixed Mode

As a non-unidirectional layup causes both mode I and mode II delamination, it consequently also has multiple SERR. G_I and G_{II} are for respectively mode I and mode II. With a mixed mode bending (MMB) test, both of these values can be estimated [30]. Unfortunately, the

errors determining the SERR can be up to 30% using linear theory [37]. Reeder et al. proposed limiting the nonlinear error by adapting the apparatus, a description can be found in ASTM D6671 [37] [38] [39].

Theoretically, an asymmetric laminate will also introduce mode III. In literature, it is common to omit any information about mode III. Although uncommon, Davidson et al. showed that $G_{III} \ll G_{II}$ for several layups [34]. This, however, was not achieved by a DCB or end-notched flexure (ENF) test, but with a single-leg bending (SLB) test.

2.4 Fibre bridging

In the lamination process, layers of fibres are stacked. It is common in UD laminates that these fibres migrate to adjacent plies during curing [40]. When fully cured, the midplane between two layers is not a straight line. Some fibres have nested themselves (slightly) into the adjacent layer. In Figure 2.2(a), a schematic illustration of two $[0°]_6$ layups can be seen which are stacked together in Figure 2.2(b). Under Mode I loading, these fibres generate a bridging effect. The fibres are located before the crack in the upper or lower layer and afterwards vice versa. Hence, these fibres are torn out of the matrix and form a 'bridge' during delamination, see Figure 2.3.

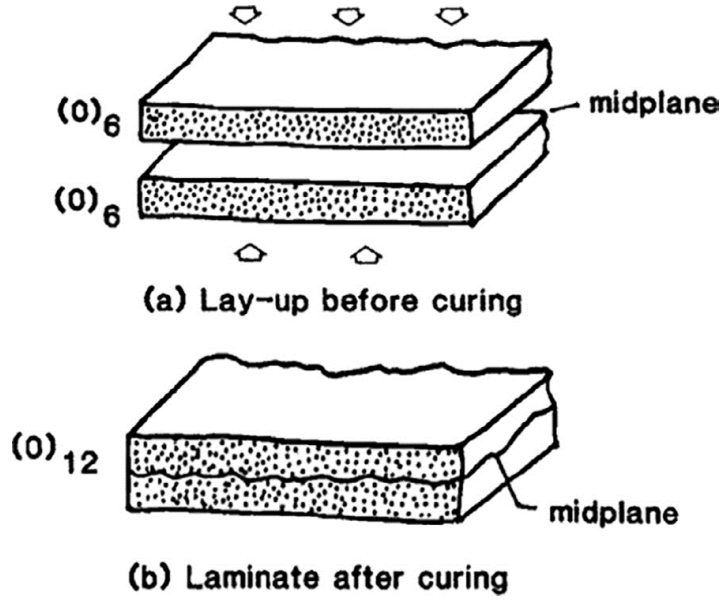

Figure 2.2: Schematic illustration of a 12 layered UD laminate, pre- and post-curing [40]

Fibre bridging has been studied over the last decades as it has the potential to improve the through-thickness material properties of an FRP [42]. First, it will improve the fracture toughness and is a reason to research for techniques which enhance the inter-laminar toughness. These techniques include stitching [43] and z-pinning [44]. On the other hand, the effect of fibre bridging makes it harder to predict under what circumstances delamination growth would pursue [45] [46]. Its crack growth behaviour is directly affected by the fibre bridging. After cutting off the bridging fibres, an increment in the delamination is noticed [42].

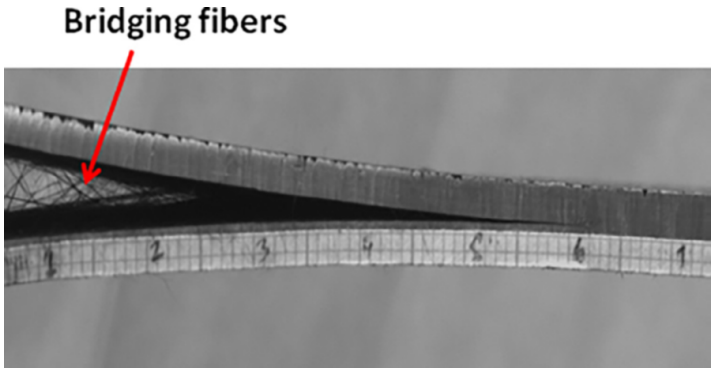

Figure 2.3: Bridging fibres during a DCB test [41]

The density of the bridged fibres varies over the fibre bridging region, with a higher density nearer to the crack tip [47]. In the beginning of a DCB test, the fibre bridge region enlarges. Whereas later on, it will move, i.e., shift towards the 'new' crack tip. Around the crack tip, a new dense fibre bridging region appears. At the other end, a decrease in density of the fibre bridging is visible. This is due to fibres that break or are pulled out from the material and no longer contribute to the bridging effect [46]. Eventually, at that location no fibres are left and the fibre bridging region is shifted along with the crack tip.

This effect can also be seen in fatigue resistance curves. In Figure 2.4, the resistance curves with increasing pre-crack lengths can be observed. A longer pre-crack corresponds to a longer fibre bridging region and the curves shift to the right. When the fibre bridging region is no longer increasing and is only shifting backwards, the resistance curves for different pre-crack lengths will coincide, as can be seen in Figure 2.4.

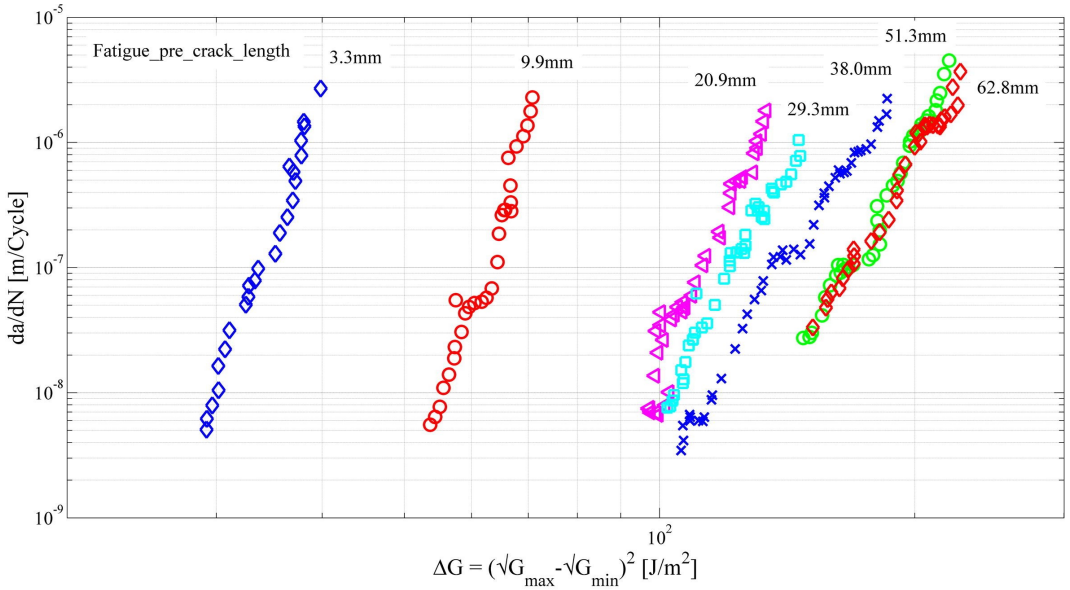

Figure 2.4: The increase in fibre bridging shown by fatigue resistance curves [48]

Fibre bridging is a mechanism which is widely studied for its beneficial aspects. Most importantly, it enhances the fracture toughness. Hu and Mai found that the fracture toughness

was increased by a factor of 9 due to fibre bridging [49]. This value may be a bit optimistic as they assumed a linear crack profile over the bridging. On the other hand, fibre bridging is not consistent along the test. The delamination resistance increases by a larger fibre bridging region. Hence, the influence of fibre bridging may cause unpredictable results.

2.4.1 Multi-directional layup

When the fibre orientation at the interface has an offset, a decrease in fibre bridging is seen. An incline of 1.5 or 3 degrees reduces the fracture toughness significantly compared to its 0 degree equivalent [40]. This implies that even for larger angles the nesting and thus fibre bridging is negligible [50]. Even though the effect of fibre bridging is decreasing rapidly when the interface angle increases, for a 3 degrees incline, the effect of fibre bridging is still (significantly) present, i.e., almost twice the bondline strength [40].

Increasing the interface angle also results in a deviation on the delamination plane [51]. Since the crack path is no longer parallel to the fibres, the delamination will continue in the adjacent plies. Figure 2.5 shows how the crack propagates towards a ply with the fibres parallel to it. As a result, the direction of the fibres and the crack propagation are parallel. This is similar to the situation of an $0°//0°$ interface and thus fibre bridging will occur. Once the adjacent ply is reached, the crack path will return back. This is repeated such that a zigzag manoeuvre is created [52]. The magnitude of this effect is primarily determined by the stiffness of both DCB arms. The oscillating bridging phenomenon was noticed to a larger extent in less stiff specimens [52].

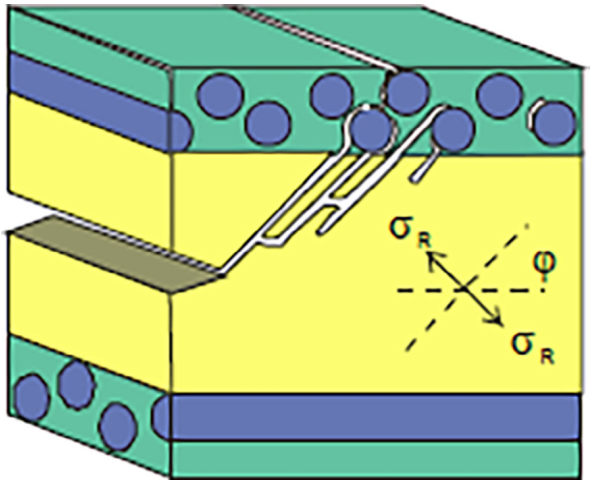

Figure 2.5: Schematic illustration of a deviation plane in a cross-ply laminate [50]

At the other end, an interface with the fibres perpendicular to the loading ($90°//90°$), a different phenomenon can be observed. As can be seen in Figure 2.6, the crack front oscillates around the $90°//90°$ interface and leaves behind a trapezoidal pattern [53]. The specimen has a $[90°/0°_{10}/90°]_s$ layup. This made it possible for the crack to migrate from one $0°//90°$ interface, through the $90°$ layers, to the next $0°$ layer. Furthermore, it can be noted that the crack does not go back and forth directly. Before migrating to the $90°$ layers, it first follows a $0°//90°$ interface for a moment [54]. In a significant number of the trapezoidal sections, both delamination planes around the $90°$ layers are delaminated simultaneously.

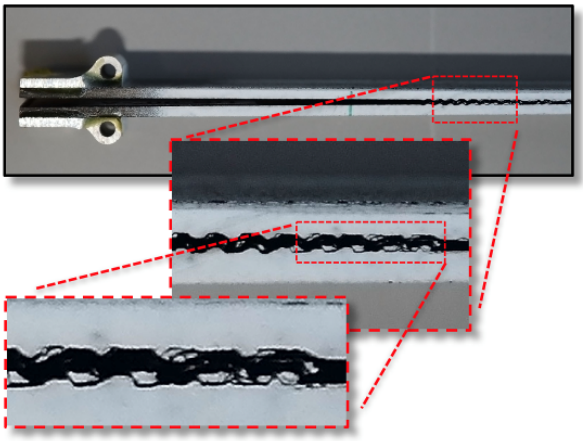

Figure 2.6: Trapezoidal delamination oscillations in a $90°//90°$ interface [54]

The same trapezoidal behaviour is seen in the fractography. At the end of the test, fibre bridging is observed in the transverse, along the 90° fibres, direction. In Figure 2.7, the loose ligaments can be observed. The fibres are clearly pulled out and appear to fluctuate from side to side.

Figure 2.7: Fibre bridging of an $90°//90°$ interface [54]

2.4.2 Fatigue

When comparing fibre bridging under fatigue and quasi-static loading, it is seen that the amount of fibre bridging is different [55] [56]. In short, the contribution of the fibre bridging is less in fatigue loading [55]. Furthermore, during fatigue the stresses in the bridging fibres

are lower than when loaded quasi-statically [56]. Moreover, fibre bridging is also affected by temperature [42]. Hence, temperature monitoring during tests is recommended to minimise these effects, especially during a test with cyclic loading .

2.5 Multi-directional fatigue

The amount of research for a multi-directional layup in combination with cyclic loading is limited. Most of the fatigue research is done with a UD laminate. But a team led by Banks-Sills investigated the fatigue propagation of multi-directional laminates [57] [58] [59] [60] [61]. They compared multi-directional laminates, stacked $0°/90°$ and $+45°/-45°$ plies, with an aluminium alloy. The crack in the composite material was found to grow slower [57]. The latter researches also used the same plies and but were mainly focused on obtaining a master-curve to counter the 'R-ratio effects' [58] [59] [61].

Yao et al. also used $+45°$, $-45°$ and $0°$ plies for a fatigue test [62]. These were used to see what the influence of fibre bridging has on a $45°//45°$ interface. With the modified Paris relation, the delamination prediction has, as they say, an acceptable agreement [62]. This sounds a bit ambiguous and should be further investigated.

2.6 Conclusion

This chapter explained the fundamentals for a better understanding of this thesis. The concepts of SERR and fibre bridging were given, e.g., the origin of fibre bridging in UD and MD laminates is different. Additionally, the design guidelines of MD lay-ups and their influences were discussed. Furthermore, from the literature study it became clear that the research with MD lay-ups in combination with fatigue delamination growth is limited. This research tries to fill that gap with an answer on the research question described in Chapter 3.

Chapter 3

Problem Description

In this chapter, the research question, including sub-questions, are stated in section 3.1. Following this, the expected result based on the literature study is given in section 3.2.

3.1 Research Question

After studying the literature in the field, it became clear that the knowledge of fatigue delamination growth for multi-directional lay-ups is limited. Even though delamination is a critical failure mode for FRP, cyclic loading of a multi-directional interface is barely studied [8]. Furthermore, the focus of most of the work that has been done is on the 'stress ratio's effect'. Hence, the knowledge of what would happen if the interface changes is minimal. Besides for a $0°//0°$ interface, it is hardly known how the delamination would behave. Therefore, the research question arises:

> *What is the influence of the fibre orientation at the interface on delamination growth rate under cyclic loading?*

The influence of the interface on fatigue delamination growth, can be observed as both the effect of changing the interface angle as well as the orientation hereof with respect to the loading. In order to answer the main question, it is crucial to have an understanding of both these influences. Accordingly, the following sub-questions are formulated:

> *What is the influence of the interface angle on delamination growth rate under cyclic loading?*
>
> *What is the influence of the orientation of the interface angle on delamination growth rate under cyclic loading?*

For the first sub-question, the objective is to find the influence of the change in angle between the adjacent interface layers. Whereas, the second sub-question maintains the interface angle as a constant, but varies the orientation of it, e.g., $(0°//\alpha)$ vs. $(0.5\alpha// - 0.5\alpha)$.

3.2 Hypothesis

Crack growth is mainly determined by the fracture toughness of the matrix material. When the SERR is higher than the critical value (G_{IC}), crack growth is initiated. Hypothetically, this is independent of how the fibres are orientated around the crack's interface as the crack "grows" through the matrix material. However, some of the energy is absorbed by bridging fibres [63]. This, in turn, would cause an increase in the critical value.

The quantity of the fibre bridging will differ for different fibre orientations [40]. Orientations closer to 0° will result in more fibre bridging. Consequently, a 0°//0° interface would give the most fibre bridging and thus would have the highest critical value, G_{IC}. This, however, does not apply to a 90°//90° interface. In case of a 90°//90° interface, a significant increase in fracture toughness is observed due to the bridging fibres [54].

In total, the amount of fibre bridging and thus the fracture toughness was determined by both the quantity of the nesting fibre and the accessibility of the crack to migrate through the adjacent layers. First, it was expected that laminates with an interface closer to 0°//0° will have more fibre bridging. For a larger difference in orientation angles between the two interface layers, the fibres obstruct adjacent fibres from nesting. Second, the crack could only migrate through layers close to an orientation of 90° with respect to the loading direction. For smaller angles, the fibres prevented the crack from migrating.

A similar effect was expected to be seen when loaded in fatigue, i.e., more fibre bridging for orientations closer to 0° or 90°. Although the fibre bridging for the same configuration is expected to be less than in the quasi-static case, it was still expected that the presence of bridging fibres would cause the measured SERR (G) to be higher than for pure matrix cracking, for the same fatigue crack growth rate (da/dN).

As can be seen, it was expected that the orientations of the interface layers are of importance for the delamination growth rate. The largest increases in the fracture toughness were expected to be seen in both an interface angle of 0° in combination with a 0° orientation and an interface angle of 0° in combination with a 90° orientation. The case of an interface angle of 90° in combination with a 0° orientation was expected to be similar to that of an interface angle of 0° in combination with a 90° orientation, except, the crack migration through the layers will be smaller, i.e., one layer instead of two.

Other combinations of interface angle and orientation of this interface angle were expected to be more or less similar, because of the restricted probabilities of fibre bridging. Whether this is caused by either the blockade of nesting or prevention of migrating. For that reason, the crack had, hypothetically, only propagated through the matrix material.

Chapter 4

Test Plan

In this chapter, the specimen designs are explained to answer the questions from the previous chapter. This is obtained by giving a description of the specimens that were tested and the reasoning of these interfaces and layups. First, in section 4.1 an overview of the different interface is given. Hereafter, the complete layups of the specimens are defined in section 4.2.

4.1 Test Matrix

To answer the research question, several tests had to be carried out. To cover "delamination growth" and "cyclic loading", DCB tests were performed on a fatigue bench. As one knows, fatigue tests take plenty of time to perform and thus the total number of test was narrowed down. Furthermore, the test can be stopped at any time as the specimen does not fail during such a test. For a displacement controlled test, the crack growth converges to a minimum.

Since the number of tests needed to be limited, a trade-off in all possible interfaces was made. First, several layups should have different interface angles. Second, the test matrix should include different orientations for the same interface angle. Last, the interface should contain more common fibre orientations, e.g., $0°//0°$ instead of $1°//1°$. As a result, seven different layups were chosen.

In Table 4.1, an overview of all the designed interfaces can be found. In the top row, the interface angles are stated in a bold font. Underneath, the different layups corresponding to that angle are presented. For the first column, the interfaces are constructed with the same fibre orientation with respect to the loading, i.e., a $0°$ angle interface. Whereas, the interfaces of the third column have a $90°$ angles between the fibres of the two adjacent layers, but with different orientations.

The tests situated in the first row, have one interface layer constant at 0 degrees and the adjacent layer changing, i.e., $0°//\alpha$. The interface angle changes according to the changing layer. Therefore, these tests represent the first research sub-question. Similarly, the columns relate to the second sub-question. In this case, the interface angle does not change, even though, the orientation is different.

Table 4.1: Overview of the designed interfaces

0 degrees	**45 degrees**	**90 degrees**
0°//0°	0°//45°	0°//90°
45°//45°		45°// − 45°
90°//90°		30°// − 60°

4.2 Specimen Layups

A non-zero B matrix introduces unwanted coupling moments. As the DCB test will be performed to analyse the results of the mode I test, one should be aware of this. Although the caused effects are mostly neglectable, the results could hypothetically be influenced. With this in mind, the specimen layups were constructed.

The layup for each laminate was determined on the basis of multiple components. First, the stacking sequence should result in a zero B-matrix. One way to achieve this is to build a symmetrical layup. This can be obtained for most of the layups. Some, however, have an interface where the adjacent sides are not identical. For these laminates, the B-matrix values were striven to be as low as possible.

Second, B_t and D_c values were also kept as low as possible. As described in section 2.3, these values determine the amount of skewness and the curvature of the G distribution. In order to reduce them, the number of zero degree layers was increased. Besides the interface, all other layers were designed to be a zero degree layer to maximise the reduction. The exceptions are the 45//45 and 45//-45 specimens.

Third, some layups were based on preliminary research by Yao [64], i.e., the specimens with an interface of 0//0, 45//45 and 45//-45. For the purpose of comparison, these layups were made identical to Yao's research.

Last, the aim was to design both the cantilever beams with approximately the same stiffness. Hence, the layup for a specimen with a $0°//\alpha$ interface looked like $[0^\circ_{16}//(\alpha/0^\circ_{15})]$ instead of $[0^\circ_{16}//(\alpha/0^\circ_{14}/\alpha)]$. Given all the points mentioned above, the following layups were designed. In Table 4.2, the layups with their corresponding B_t and D_c values are listed how they were tested. The layups are tested upside down in comparison with the designed layups. Consequently, the crack propagation is mirrored. This, however, has no further consequences in terms of results. During the test, the interface (as in the specimen's name) was seen from below. Therefore, the results of both layups are identical.

Table 4.2: Overview of the designed interfaces with their corresponding layups in the tests

Interface	Layup	B_t	D_c
0//0	$[0^\circ_{16}//0^\circ_{16}]$	0	0.004
45//45	$[(\pm 45°/0^\circ_{12}/\mp 45°)//(\pm 45°/0^\circ_{12}/\mp 45°)]$	0.006	0.08
90//90	$[(0^\circ_{15}/90°)//(90°/0_{15})]$	0	0.004
0//45	$[0^\circ_{16}//(45°/0_{15})]$	$3 \cdot 10^{-5}$	0.004
0//90	$[0^\circ_{16}//(90°/0_{15})]$	0	0.004
45//-45	$[(\pm 45°/0^\circ_{12}/\mp 45°)//(\mp 45°/0^\circ_{12}/\pm 45°)]$	0	0.08
30//-60	$[(0^\circ_{15}/30°)//(-60°/0^\circ_{15})]$	$2 \cdot 10^{-5}$	0.004

As can be seen in Table 4.2, each specimen has 32 layers. This resulted in specimens with a thickness of approximately 5.2 mm. Hence, for the calculations of B_t and D_c, a ply thickness of 0.16 mm is used. Furthermore, the width and length of each specimen is respectively 25 and 200 mm.

Chapter 5

Experimental Methodology

In this chapter, an explanation of the methodology of this research is given. First, a description of the manufacturing of the specimens is given in section 5.1. This is followed by the experimental set-up in section 5.2. Finally, the analysing processes are discussed.

5.1 Specimen Manufacturing

Before testing, the specimens had to be manufactured. As mentioned in Chapter 4, seven different layups were tested. Hence, seven different laminates were manufactured. These laminates were large enough to contain at least three or four specimens of 200x25 mm. For the $0°//0°$, $45°//45°$ and $45°//-45°$ laminates three specimens were manufactured and four specimens for the others layups. Although the laminates had different lay-ups, all of them consisted of 32 plies with a Teflon inserted in the midplane. The tests were performed with a CFRP, namely, M30SC/DT120 [65]. This is a prepreg which was stacked by hand, followed by curing in an autoclave. It should be noted that the prepreg was already three months past the expiration date.

Each ply was laid by hand. When a stack of four plies was reached, it was put on a vacuum table to debulk. Two of these stacks were then put on top of each other and again debulked on the vacuum table. In this way, it was made sure that all the air was out of the laminate. This process was repeated until the laminate consisted of 16 layers, half of the total laminate. Before the two halves were connected, a 0.01 mm thick Teflon film was placed on top of one of the halves [66]. Hence, the Teflon film was located between them. The Teflon film was cut to a length of 60-65 mm. This induced a pre-crack of approximately 50 mm as the edges of the laminate were cut off, because they had not the desired quality. The width of the film is not specified as long as it covers the whole laminate width. It was made sure that it stuck out on both sides to clearly distinguish were the crack should start.

Next, the laminates were prepared for the autoclave, i.e., it was vacuum bagged. Both sides of the laminate had a peel ply layer in order to reduce surface treatments for the attachment of the aluminium blocks later on. Furthermore, only one side had a smooth surface, i.e., the

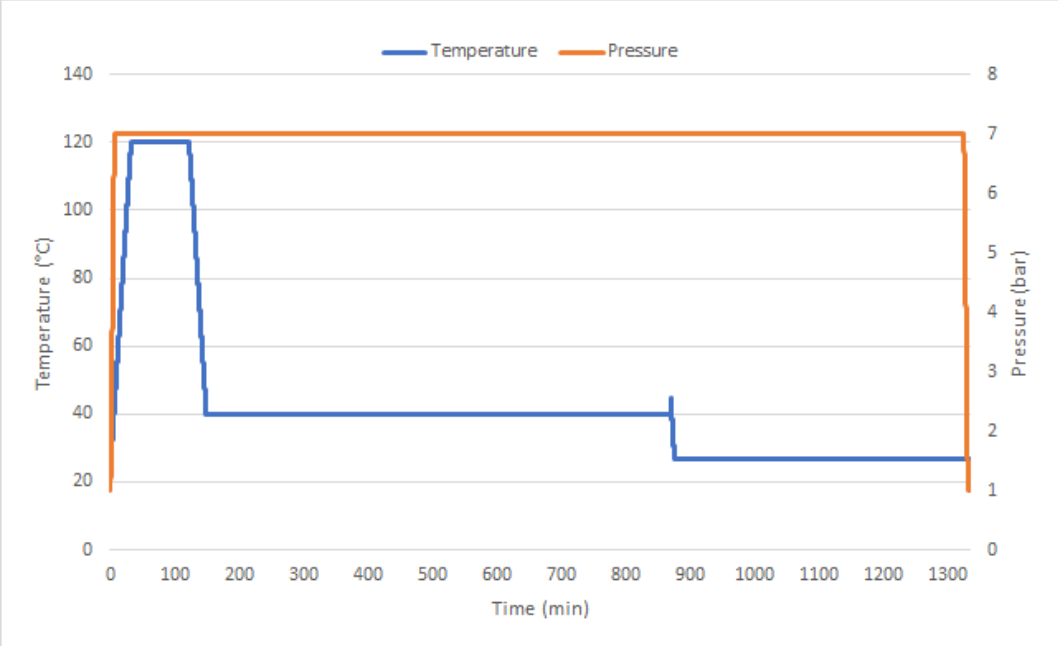

Figure 5.1: Autoclave cycle of the curing process

side facing the mould. The other surface was formed by a breather in combination with the vacuum and pressure from the autoclave as it did not require a smooth surface.

All the seven laminates went simultaneously inside the autoclave and were cured and post-cured. The curing was realised by a temperature of 120°C at a pressure of 6 bar for 90 minutes. Hereafter, it was cooled to 40 degrees and this was kept for 700 minutes. This process happened overnight and the temperature was reduced manually in the morning by the laboratory staff. In Figure 5.1, the (post) curing process is shown.

After curing, the laminates underwent a C-scan to see any imperfections and whether all the protection films were removed from the plies. In Figure 5.2, a C-scan of the 30//-60 laminate is shown. The Teflon, the large black area on the right, is clearly visible. Also, the thickness of the laminate narrows down towards the edges, thereby, the magnitude of the scan signal becomes larger. In the next step of the manufacturing process, these were eliminated to maintain a constant thickness over the specimen. The main purpose of the C-scan, however, was to see any imperfections. Even though many reddish to black areas can be seen, it does not mean the laminate is full of imperfections such as voids. These areas are visible due to the laminate's rough surface. The C-scans of the other laminates are located in section A.1.

The laminates were cut with a diamond saw into specimens of 200x25 mm. The saw itself was a bit inaccurate, so the specimens were defined to be a bit wider. To make sure they would fit into the moulds of the load introduction blocks, the last (tenths of) mm was removed with sandpaper. Now, the specimens had the right dimensions of 200x25 mm, the last step before testing could be carried out. The aluminium blocks were attached to the specimens. First, the blocks were sandblasted. Second, the peelply was taken off the specimen and the 3M Scotch-Weld epoxy adhesive EC-2216 B/A was applied [67]. Last, the specimens and blocks were joined together. After 24 hours of curing, the specimens were ready for use.

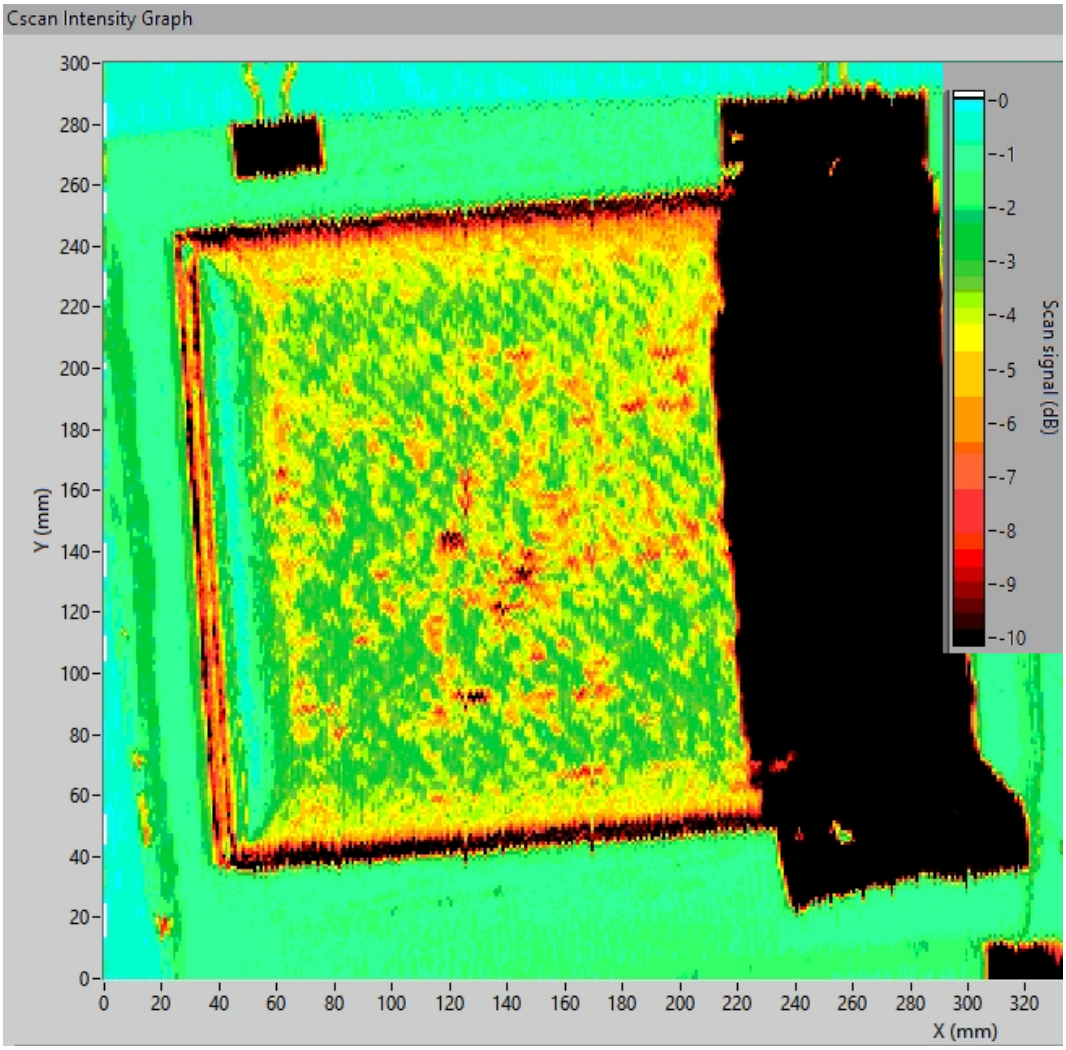

Figure 5.2: C-scan of the 30//-60 laminate. Note: the dimensions on the X- and Y-axis are not to scale.

5.2 Experimental Set-up

In order to realise Mode I delamination, DCB tests were performed. For this, a MTS 100 kN fatigue testbench with a 1 kN loadcell was used. This machine, along with the other necessary equipment, is available at the Delft Aerospace Structures and Materials Laboratory (DASML). One of the equipment is a camera car, i.e., a camera connected to a computer from which it is controlled and the taken images were stored. This can be connected to the testbench as well. From here, it is regulated when the camera has to make an image. For the first 5000 cycles, an image was taken every 100 cycles. For the range of 5000 to 20000 cycles, the images were taken with an interval of 500 cycles and from 20000 cycles till the end of the test, every 1000 cycles, according to the test standard of Alderliesten and Brunner [68].

Due to an asymmetric lay-up, it is of interest whether the crack propagates on both sides with the same rate. Hence, two cameras were chosen to cover both sides of the crack. This, simultaneously, resulted in two lights, i.e., one for each side.

First, the specimen was loaded quasi-statically, with a loading rate of 1mm/min, to determine the fracture toughness, G_{Ic}. For the first test, the loading was stopped directly after noticing crack propagation. The corresponding cross-head displacement was obtained and taken as δ_{max} for the fatigue loading [68]. The tests were performed with a load ratio of R = 0.1 at room temperature. This means that the δ_{min} was initially taken as:

$$\delta_{min} = 0.1 \cdot \delta_{max} \tag{5.1}$$

to make it correspond with a displacement ratio of $R_d = 0.1$. This, however, was not equal to the load ratio of $R = 0.1$. Hence, the minimum displacement was adjusted in order to meet the required load ratio:

$$R = \frac{P_{min}}{P_{max}} = 0.1 \tag{5.2}$$

For the first 100 cycles, the δ_{min} was adjusted such that the load ratio was $R = 0.1$. For the next 100 cycles, it was made sure that a maximum deviation of 10% of this load ratio was maintained.

Each specimen was tested twice. One, just after the pre-crack created by the Teflon film, and one, further on. Before the second test, the crack was extended quasi-statically with a loading rate of 1 mm/min in order to have a larger pre-crack. In this way, it was made sure that the amount of fibre bridging in the second test was significantly more saturated than in the first test. For the second test, the value of δ_{max} was taken at the end of the quasi-static crack increase.

Unfortunately, the testbench is not capable of running a large displacement (>5 mm) in combination with a high frequency (5Hz). This resulted in a longer test duration for the same amount of cycles, as the frequency was lowered. For these tests, the frequency was kept as high as possible to attain a larger number of cycles in the same time span. The second test with a longer pre-crack was often started during the weekends, as the frequency could be reduced. In Appendix B, an overview of the tests with the their frequency and total cycles is given.

Prior to the tests, the accuracy of the loadcell was determined with weights. The weight was first determined with a scale before weighing at the loadcell. The weights were hung

under the loadcell with the use of cable ties, whose weights were also determined with the scale. In Table 5.1, the combined weight is given from the measurements of both the scale and the loadcell. Note: the measurements form the scale are converted to Newtons using the gravitational acceleration constant of $g = 9.81\ m/s^2$.

Table 5.1: Weights measured with a scale and loadcell

Load	Scale (N)	Loadcell (N)	Difference (|N|)
500 gr	4.96	5.27	0.31
1 kg	9.86	9.80	0.06
2 kg	18.64	18.93	0.29
5 kg	49.06	49.64	0.58
10 kg	98.17	98.31	0.14
15 kg	147.25	147.61	0.36

In Table 5.1, it can be seen that the measured values of the weights are similar. All values are within ±0.6 N of each other. Therefore, for this research, the values measured by the loadcell are considered accurate and was used without any correction.

5.3 Post-Test Analysis

The data retrieved from the testbench itself does not mean anything. It has to be analysed. The obtained data were converted into graphs. In addition, the crack front and surface were also observed.

5.3.1 Data Analysis

The data from the machine is not the end result. The raw data captured by the testbench had to be processed to give workable results. Additionally, the cameras made pictures, from which the delamination lengths had to be determined. Every couple of cycles as described in the previous section, an impulse was given for the capture of a picture. Therefrom, the delamination length was determined using a program called "imageJ". For every picture, the crack length was measured based on the reference grid. In total, a single picture represented the crack length of the specimen after a given number of cycles.

Not only was a signal given to the camera to make a photo, but another signal was also sent to capture the displacement and force data at that moment. This data was transferred in the form of voltage from one computer to another. Hence, the displacement and the force could be easily coupled with the crack length. In conclusion, the required variables are simultaneously given for the SERR calculation using the modified compliance calibration (MCC) method as described in ASTM D5528 [11]:

$$G = \frac{3P^2C^{2/3}}{2mbh} \tag{5.3}$$

In here, P is the load, C is the compliance, b is the specimen width, a is the delamination length and m is the slope of the modified compliance calibration. This was obtained by

plotting a by thickness normalised delamination length (a/h) versus the cube root of the compliance ($C^{1/3}$) and from this a least squares regression fit was calculated.

In addition, for the fatigue delamination growth rate (da/dN), a 7-point incremental polynomial method was used as described in ASTM E647 [69]. This method uses a second order polynomial fitting to seven consecutive data points. Therefrom, the derivative is taken and the da/dN value is calculated accordingly. In the end, the resistance curves were constructed by plotting this delamination growth rate as a function of the SERR.

5.3.2 C-scan

After the end of the second test of the specimens, but before the fractography, a C-scan was performed. It was performed to determine the crack front at the end of the test. The specimens were hung in a bath of water with the opening downwards. The specimens were oriented as such that the image shows the specimen as if it is seen from the topside during the test. After the specimen was hung in place, a probe moved with a speed of 200 mm/s from the top to the bottom. This was done a multiple times, as every top to bottom movement has captured a width of 1 mm. Aligning all the stripes, an image was created.

5.3.3 Fractography

After each test was performed, the specimens were torn apart in order to observe the crack surface. Some were already split in the test bench itself due to lack of oil pressure. This resulted in piston that gradually moved downwards resulting in a high force that could not be withstood by the specimen. Because of this, the crack in the specimen continued to increase in an uncontrolled manner. Consequently, the specimen broke before a C-scan could be made. Furthermore, no picture were made of the bridging fibres during the rupture process.

Following this, after the C-scan, the specimens were put back on the testbench. This time, the displacement was increased manually. A displacement extension of approximately 4 mm/min was applied. Every couple of seconds, it was paused to take an image of the crack opening, until the specimen had become two separate cantilever beams. These were then placed on a white background and thoroughly examined.

Chapter 6

Results

In this chapter, the results of this research are shown. First, in section 6.1, the data representation is explained. Second, the resistance curves are presented. After that, the crack itself is studied by means of C-scan after the test, fibre bridging during and after the test, and the fracture surface.

6.1 Crack Growth

From all the pictures captured by the camera, the crack length was determined as described in subsection 5.3.1. From this, the crack growth was calculated in order to generate a resistance curve. In Figure 6.1, the results of the 0°//0° specimens are shown. Here, four clouds of dots (dashes and diamonds) can be distinguished, each cloud representing one fatigue test.

A little smaller, each small dash (-) and diamond ($\diamond$) visualises the result of one data point. This was done every couple of cycles. After a certain amount of cycles, a picture was taken and the corresponding load and displacement values were captured, see Chapter 5. The data was processed, as mentioned before, and it is shown in the graph. This was done multiple times per fatigue test and, as a result, a bunch of data points were drawn.

For each test, a lot of data points was generated. Collecting all of them in a single plot, resulted in a cloudy mess. It was already hard to distinguish the tests 0//0-2.2 and 0//0-3.2 data presented in Figure 6.1. In order to compare the different data with each other, a power curve was fitted. This made it easier to distinguish different resistance curves.

Each specimen is represented by either a dash or a diamond. The first specimens are represented with dashes, whereas the second specimen diamond. Thus, the first and second tests of the same specimen are drawn with the same symbol. Hereafter, the specimen was replaced and the process was repeated. For this, the data point is marked with another symbol.

As already mentioned, each specimen had two tests. One, right after the Teflon insert and the other one, later on. In the graph, the first tests are shown as uninterrupted lines and the second tests are visualised as dashed lines. In Figure 6.1, the two dashed lines of the second

tests are very similar. In order to distinguish them, the lines of the second specimen have diamonds at the end.

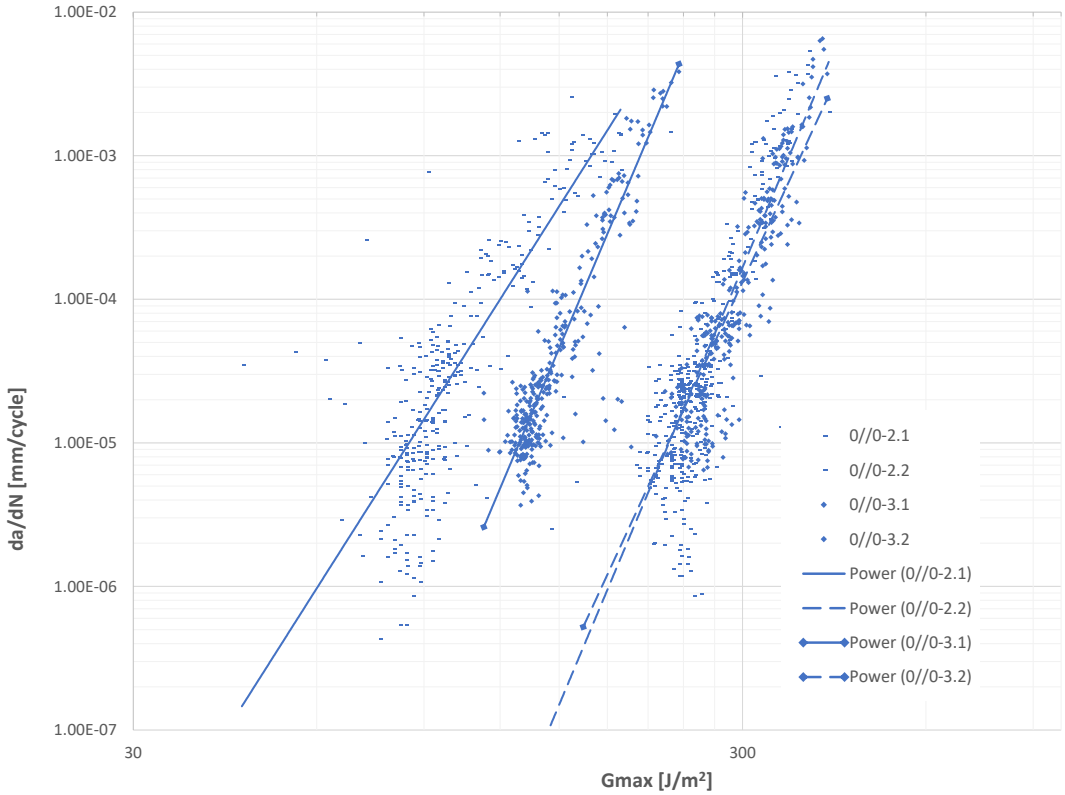

Figure 6.1: da/dN vs Gmax graph of the 0°//0° interface.

The data of test 0//0-2.1, in Figure 6.1, shows a sort of kink. The top half of the data correlates in a certain manner, whereas, around approximately $1.00 \cdot 10^{-04}$ mm, the data has a much steeper correlation. This, however, is not possible to catch in a single regression curve. The power curve has a best fit over all the data and appears linear in a log-log plot.

The data in Figure 6.1 should be read in combination with the beginning crack length of the test, the data on its own does not say anything. As already mentioned before, the first test started with a different initial crack length (a_0) than the second test. However, the begin crack length of each layup is more or less constant. The Teflon film insert has created a uniform initial crack, see also Figure 5.2. Hence, crack propagation after quasi-static loading for the first test is observed to be around the same crack length.

In Table 6.1, the crack length of the 0°//0° specimens after 100 cycles is given. Within the first 100 cycles, the loading was adjusted to meet a load ratio of 0.1. Hereafter, the test was run with displacement values such that the load ratio was within an accuracy of 10% of 0.1.

For the two first tests, a larger initial crack length corresponds to a larger SERR. The curve of test 0//0-3.1 has shifted to the right compared to test 0//0-2.1. Furthermore, both the second tests, which have a larger initial crack, have an increase in fracture resistance. On the other hand, the increase in crack length after 100 cycles of test 0//0-2.2 with respect to test 0//0-3.2, does not show any significant difference in resistance curves.

Table 6.1: Crack lengths of $0°//0°$ specimens after 100 cycles

Specimen	Crack length (mm)
0//0-2.1	48.399
0//0-2.2	114.322
0//0-3.1	55.38
0//0-3.2	105.503

The results of the other specimens can be found in section C.1. For the remaining part of this chapter, only the regression curves are shown. This makes it easier to compare the results. It should be noted that the fitting of the regression curve of 0//45-1.1 could have been better. It is determined with the same fitting power function as the other regression curves. Moreover, the colour of these curves matches the colour of the same specimen in section C.1.

The da/dN vs G_{max} plots were constructed with the use of one camera, whereas two were installed. As each were capturing a single side of the specimen, the crack propagation could be monitored from both sides. For the calculation of da/dN and G_{max}, however, only one crack length is required. Hence, the shown data was determined with the use of a single camera, i.e., the camera in which the crack propagates to the right. In order to determine whether the crack propagated consistently, every 50 pictures the crack length of both cameras was compared and the difference was calculated. These differences of the 0//0 specimens are shown in Table 6.2. For the other specimens, the differences can be found in section C.2.

Table 6.2: Differences in crack length of $0°//0°$ specimens every 50 cycles

Photo	Difference in cracklength (mm)			
#	0//0-2.1	0//0-2.2	0//0-3.1	0//0-3.2
1	1.743	-0.545		-0.188
51	1.651	-1.077		-0.59
101	-0.554	-0.46		-0.66
151	-0.067	-0.75		-1.13
201	-0.371	0.047		-0.842
251	-0.515	-0.538		-0.837
301	-0.373	-0.455		-1.09
352		-0.053		
402		-0.019		

As can be seen in Table 6.2, the crack propagates similarly on both sides. With some exceptions, the difference in crack length between both sides is within 1 mm. Furthermore, larger outliers can be found at the beginning of test 0//0-2.1, this difference was between the 1.5 and 2 mm. In comparison with other symmetric layups, this number is relatively small. Although they have also a symmetric layup, the crack lengths of these specimens are dissimilar. For test 90//90-2.2,for example, the difference in crack front length varied from 4.88 to -3.885 mm.

6.2 Comparison with Multiple Interfaces

In order to answer the research question(s), the data of various interfaces have to be generated. In the previous section, it is shown how the regression curve is related to the data. In this section, the resistance curves of different interfaces are plotted in a single graph.

All the interfaces that are tested can be found in section 4.1. An overview of all the interface angles is given in Table 4.1. This table is shown in the following subsections with a single axis highlighted. The regression curves of the highlighted interfaces are then plotted in a single graph.

For the first subsection, subsection 6.2.1, the results of the specimens, which have one interface layer at 0 degrees and the adjacent layer changing, are presented. This is continued by the 0 degree interface angles in subsection 6.2.2. Additionally, the resistance curves of the 90 degree interfaces are shown in subsection 6.2.3.

6.2.1 $0°//\alpha$

In Figure 6.2, the results of the interfaces highlighted in Table 6.3 are given. As can be seen, the interfaces in the top horizontal row are tested, i.e., the interfaces with $0°//\alpha$. In this row, the interface angles change while keeping one interface layer constant at an orientation of 0 degrees.

Table 6.3: Overview of the tested interfaces

0 degrees	45 degrees	90 degrees
$0°//0°$	$0°//45°$	$0°//90°$
$45°//45°$		$45°//-45°$
$90°//90°$		$30°//-60°$

The data of the $0°//0°$ specimens was already displayed in Figure 6.1. From this, only the regression curves are taken, and in this section, it is complemented with the regression curves of the $0°//45°$ and $0°//90°$ specimens. The curves of the $0°//0°$, $0°//45°$ and $0°//90°$ specimens are depicted by respectively, blue, yellow and grey.

The results in Figure 6.2 should be seen in combination with the crack length after 100 cycles described in tables, Table 6.4, Table 6.5 and Table 6.12, for specimens with an interface of $0°//0°$, $0°//45°$ and $0°//90°$ respectively.

For all the first tests in general, the longer the precrack length, the further the resistance curve is to the right. The $0°//45°$ specimens show an exception to the other lines. Their first tests, the left bottom in the graph, shows the same trend. The slopes, however, are steeper or gentler. Hence, the other ends of the graphs are unrelated to the initial crack length.

It can be seen in Table 6.4, Table 6.5 and Table 6.12, that for both the $0°//45°$ and $0°//90°$ specimens, the difference between the first and second initial crack length is smaller than for the $0°//0°$ specimens. Nevertheless, the resistance curves of these specimens have a larger shift to the right in Figure 6.2 than the $0°//0°$ lines.

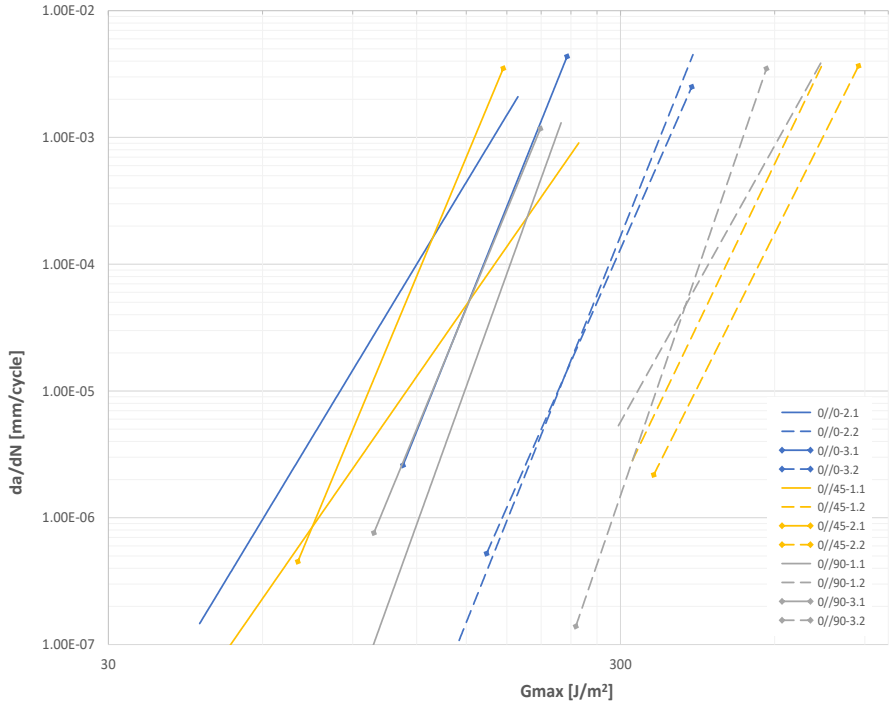

Figure 6.2: Resistance curves of different interface angles.

Although the second tests of the 0°//0° specimens align, the crack length after 100 cycles have almost a 10 mm gap. This is seen to a lesser extend for the other two layups. The start of the 0//90-1.2 and 0//90-3.2 test graphs (top right) indicate a larger SERR for the same crack growth when the initial crack is larger, even though they show dissimilarities in the slope. For test 0//45-2.2, the initial crack length is shorter than test 0//45-1.2, while the opposite is seen in Figure 6.2. Here, test 0//45-2.2 is further to the right.

Table 6.4: Crack lengths of 0°//0° specimens after 100 cycles

Specimen	Crack length (mm)
0//0-2.1	48.399
0//0-2.2	114.322
0//0-3.1	55.38
0//0-3.2	105.503

Table 6.5: Crack lengths of 0°//45° specimens after 100 cycles

Specimen	Crack length (mm)
0//45-1.1	48.273
0//45-1.2	76.947
0//45-2.1	49.062
0//45-2.2	72.401

Table 6.6: Crack lengths of 0°//90° specimens after 100 cycles

Specimen	Crack length (mm)
0//90-1.1	54.269
0//90-1.2	84.21
0//90-3.1	53.761
0//90-3.2	72.468

6.2.2 0° Interface Angle

In this section, the data of the interfaces with a 0 degree interface angle is presented. As can be seen in Table 6.7, the specimens are vertically displayed instead of horizontally as in the previous section. Here, the interface angle does not change, but the orientation does. Once again, the 0°//0° interfaces are presented, but in conjunction with the 45°//45° and 90°//90° specimens.

Table 6.7: Overview of the tested interfaces with the 0 degree column highlighted

0 degrees	**45 degrees**	**90 degrees**
0°//0°	0°//45°	0°//90°
45°//45°		45°// − 45°
90°//90°		30°// − 60°

The resistance curves of 0° interface angles with different orientations are plotted in Figure 6.3. Furthermore, their corresponding crack lengths after 100 cycles can be found in Table 6.8, Table 6.9 and Table 6.10 for the 0°//0°, 45°//45° and 90°//90° interfaces, respectively.

When each layup is considered separately, a longer precrack corresponds to a resistance curve that is more to the right. This, however, is not the case when comparing the different laminates with each other. For example, test 90//90-1.1 has a similar resistance curve in comparison with both the second 0°//0° specimens, despite having significantly smaller initial crack length. Moreover, test 90//90-1.2 is the furthest to the right.

The slopes of all the graphs are more or less the same. Only the beginning and end values of the line are oddly generated with the use of excel. It can be clearly seen in section C.1 that the data of tests 45//45-2.1 and 45//45-3.1 starts with similar fatigue crack growth rate (da/dN). While they are shown in Figure 6.3 with a significant difference.

Table 6.8: Crack lengths of 0°//0° specimens after 100 cycles

Specimen	Crack length (mm)
0//0-2.1	48.399
0//0-2.2	114.322
0//0-3.1	55.38
0//0-3.2	105.503

Table 6.9: Crack lengths of 45°//45° specimens after 100 cycles

Specimen	Crack length (mm)
45//45-2.1	44.105
45//45-2.2	78.459
45//45-3.1	45.775
45//45-3.2	74.325

Table 6.10: Crack lengths of 90°//90° specimens after 100 cycles

Specimen	Crack length (mm)
90//90-1.1	55.745
90//90-1.2	97.261
90//90-2.1	57.542
90//90-2.2	76.746

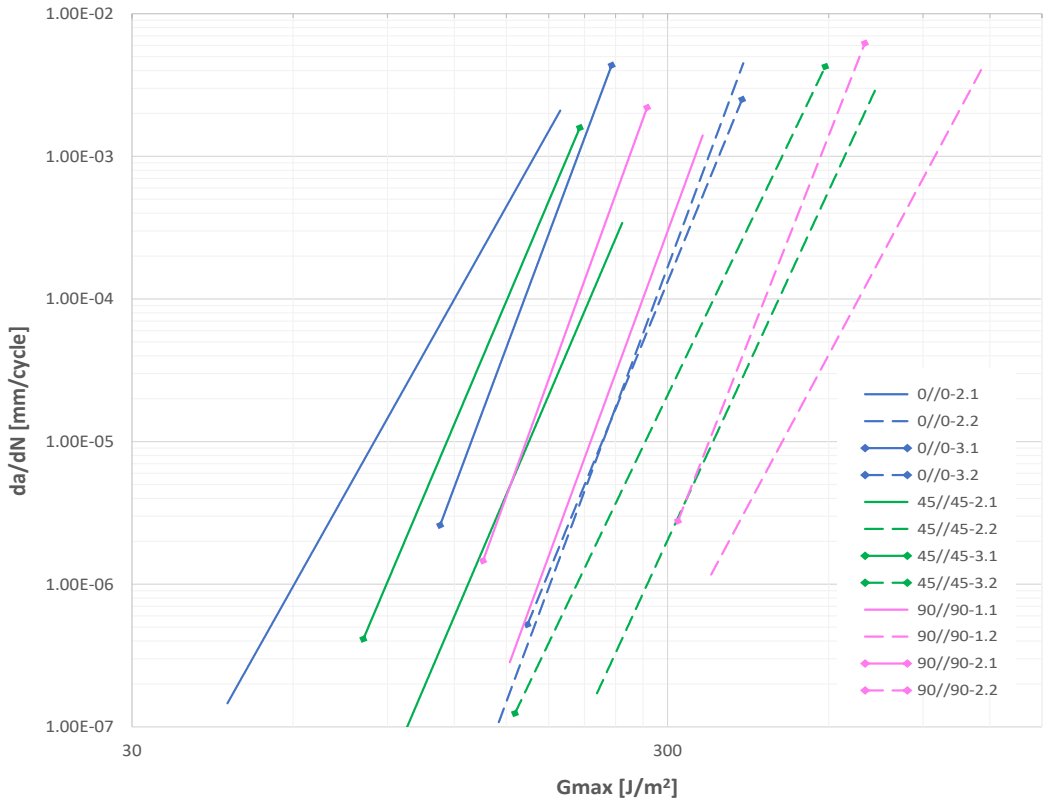

Figure 6.3: Resistance curves of 0° interface angles with different orientations.

6.2.3 90° Interface Angle

The data of the 90 degree interface angle is analysed in the same way as the specimens with a 0 degree interface angle. First, in an overview is indicated which laminates are presented in this section, see Table 6.11. The highlighted column went from the first to the last one, top to bottom. All the laminates with a 90 degree interface angle are shown in Figure 6.4. The $0°//90°$ specimens discussed in subsection 6.2.1, are complemented with the $45°//-45°$ and $30°//-60°$ laminates in this section.

Table 6.11: Overview of the tested interfaces with the 90 degree column highlighted

0 degrees	45 degrees	90 degrees
$0°//0°$	$0°//45°$	$0°//90°$
$45°//45°$		$45°//-45°$
$90°//90°$		$30°//-60°$

The crack lengths after 100 cycles, corresponding to the laminates shown in Figure 6.4, can be found in Table 6.12, Table 6.13 and Table 6.14 for respectively the $0°//90°$, $45°//-45°$ and $30°//-60°$ interface. As can be seen in Table 6.14 and Figure 6.4 the data of test 30//-60-1.1 is not present due to missing photos and thereby having undetermined crack lengths.

In Figure 6.4, one can distinguish two clusters of lines. One with all the first tests and one with

all the second tests. Although 45//45-2.1 is a first test, it relates more with the second tests of the specimens. Furthermore, the initial crack length of 45//45-2.1 is not the explanation for this shift to the right.

Both the second tests of the $0°//90°$ and $45°// - 45°$ specimens cross each other. In section C.1, the data points of these specimens are presented in respectively Figure C.2 and Figure C.4. The data points show a different correlation and the regression curves match these data. Both the 0//90-1.2 and 45//-45-2.2 resistance curves start further to the right when compared to tests 0//90-3.2 and 45//-45-3.2 respectively. Thereafter, the data points overlap and become one bunch of points. The result is a more rapid decrease of SERR for the same decrease in the fatigue crack growth rate. Hence, the slope of the curves vary.

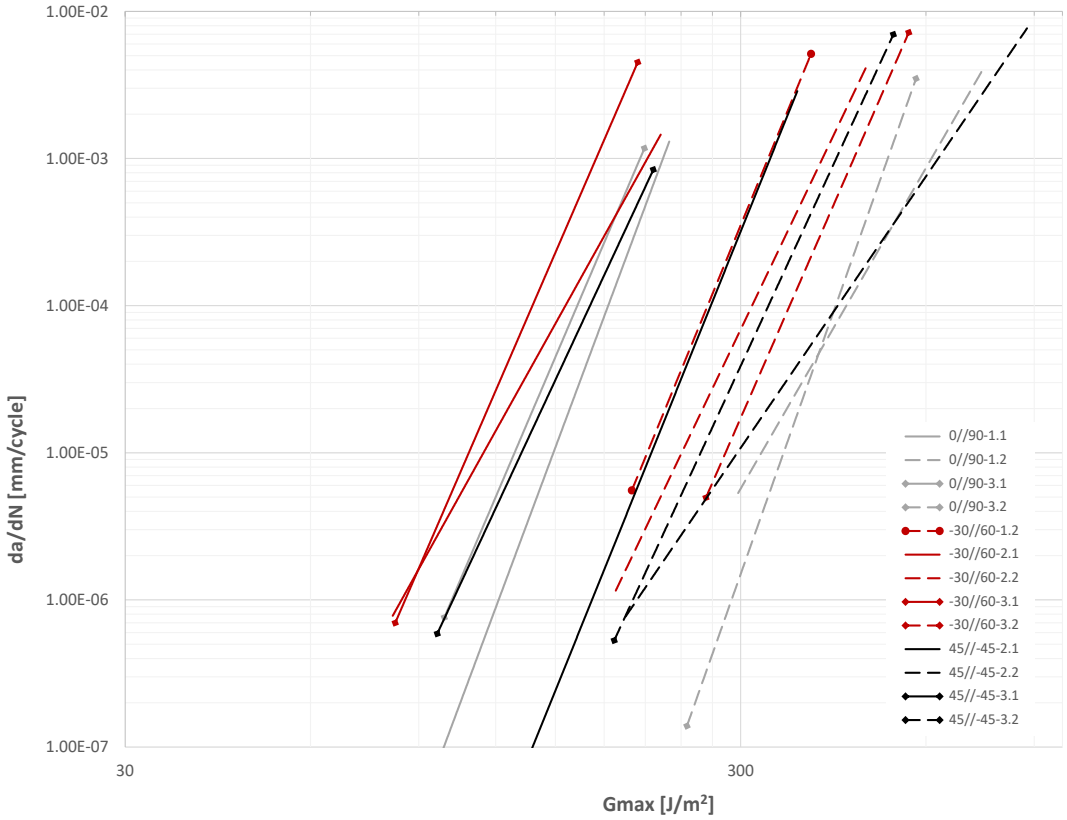

Figure 6.4: Resistance curves of $90°$ interface angles with different orientations.

Table 6.12: Crack lengths of $0°//90°$ specimens after 100 cycles

Specimen	Crack length (mm)
0//90-1.1	54.269
0//90-1.2	84.21
0//90-3.1	53.761
0//90-3.2	72.468

Table 6.13: Crack lengths of $45°// - 45°$ specimens after 100 cycles

Specimen	Crack length (mm)
45//-45-2.1	58.505
45//-45-2.2	78.459
45//-45-3.1	60.796
45//-45-3.2	70.044

Table 6.14: Crack lengths of $30°//-60°$ specimens after 100 cycles

Specimen	Crack length (mm)
30//-60-1.2	73.055
30//-60-2.1	55.642
30//-60-2.2	73.254
30//-60-3.1	54.562
30//-60-3.2	82.523

6.3 C-scan

The C-scan was conducted for most of the specimens, the rest was unfortunately already torn apart due to several reasons described in subsection 5.3.2. From the remaining specimens a C-scan image is made. In Figure 6.5, the C-scans of all the different layups are presented. Each layup is shown once, as different specimens from the same layup have similar resulting crack fronts. The C-scan results of the other specimens can be found in section A.2.

The C-scan is conducted in such a way that the top of the specimens, in the images, are facing the reader. Furthermore, the location where the Teflon films were inserted are shown in the lower area of each image, see Figure 6.5h. This implies that the crack propagated from the bottom end towards the top. Hence, the black area illustrates the crack opening, see Figure 6.5h. Simultaneously, the upper boundary of the black area represents the crack front. Furthermore, the crack itself is not always shown continuously. For most of them the upper and lower beams appear to be locally attached to each other. Especially, in the areas where the Teflon film is located. At the bottom of the images, the aluminium load block can also be seen, see Figure 6.5h.

The crack front of the 0//0-3 specimen is more or less straight along the width. It is perpendicular to the fibre direction. Likewise, specimens 45//45-3 and 45//-45-3 show a similar crack front. In contrast to specimen 0//0-3, for these specimens the crack propagation is not perpendicular to the fibres. For the 0//45-2 specimen which has one less 45° layer, the crack front is deflected towards the 45° fibres. The deflection is not a perfect 45° angle, but between a 45° angle and perpendicular to the propagation direction.

The crack front of specimen 30//60-2 is similar to the specimen 0//45-2 crack front. It is mainly affected by the $-60°$ layer. For roughly 80% the $-60°$ layer is predominant to the crack front, this is followed by a kink. Hereafter, the the crack front tends to follow the 30° layer. Although the angle between the fibres of both the adjacent interface layers is 90°, the kink is at an obtuse angle. Moreover, the interfaces with a 90° layer in them, i.e., $0°//90°$ and $90°//90°$, show a kink as well. However, this time, the kink is located more to the middle. The crack front on the edges is in front of the middle part.

6.4 Fibre Bridging

At the end of the test, the displacement was manually increased until each specimen became two parts. During this increasing displacement, photos of the specimens were taken. This

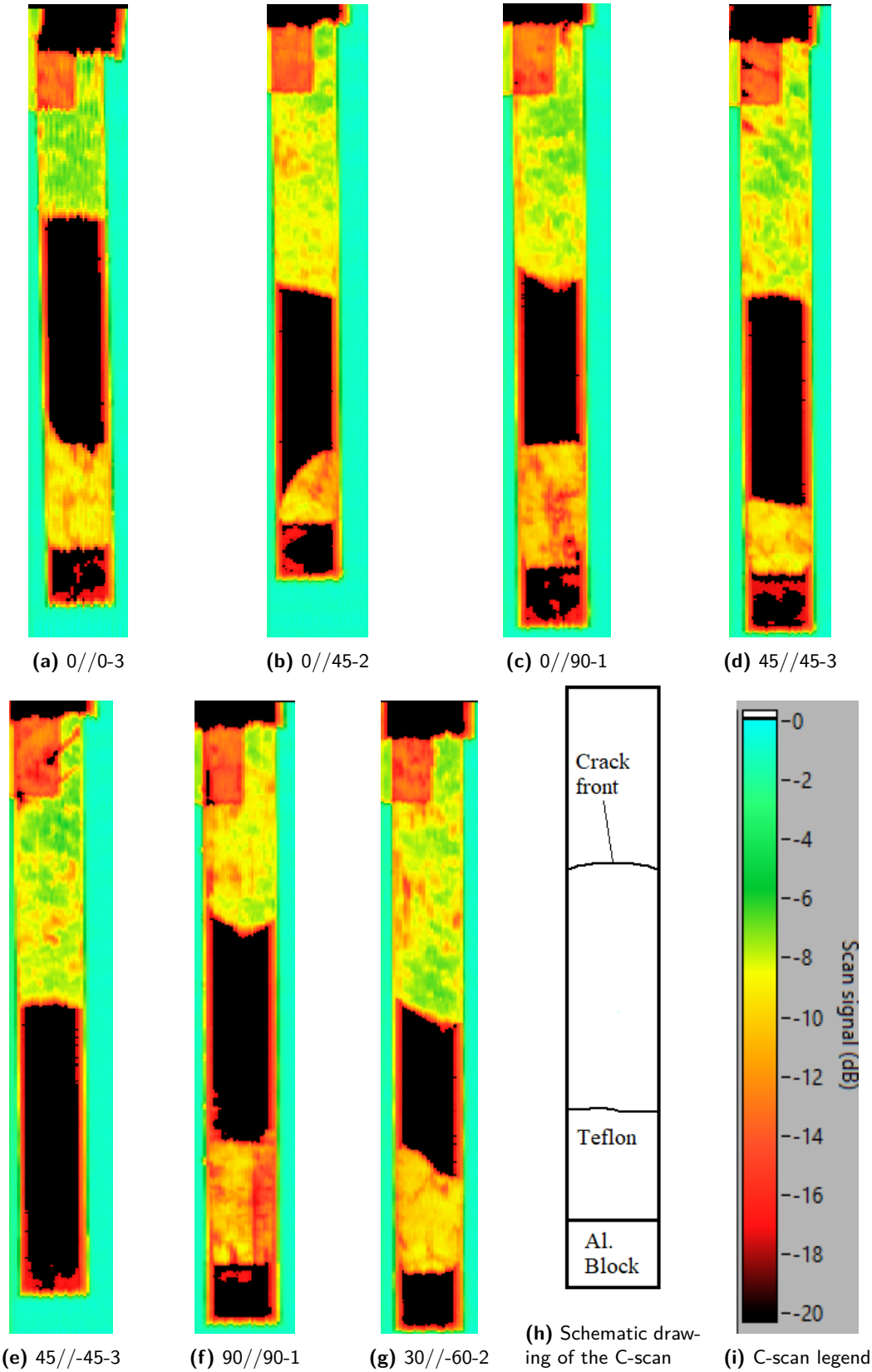

(a) 0//0-3 **(b)** 0//45-2 **(c)** 0//90-1 **(d)** 45//45-3

(e) 45//-45-3 **(f)** 90//90-1 **(g)** 30//-60-2 **(h)** Schematic drawing of the C-scan **(i)** C-scan legend

Figure 6.5: C-scan of the specimens after the test

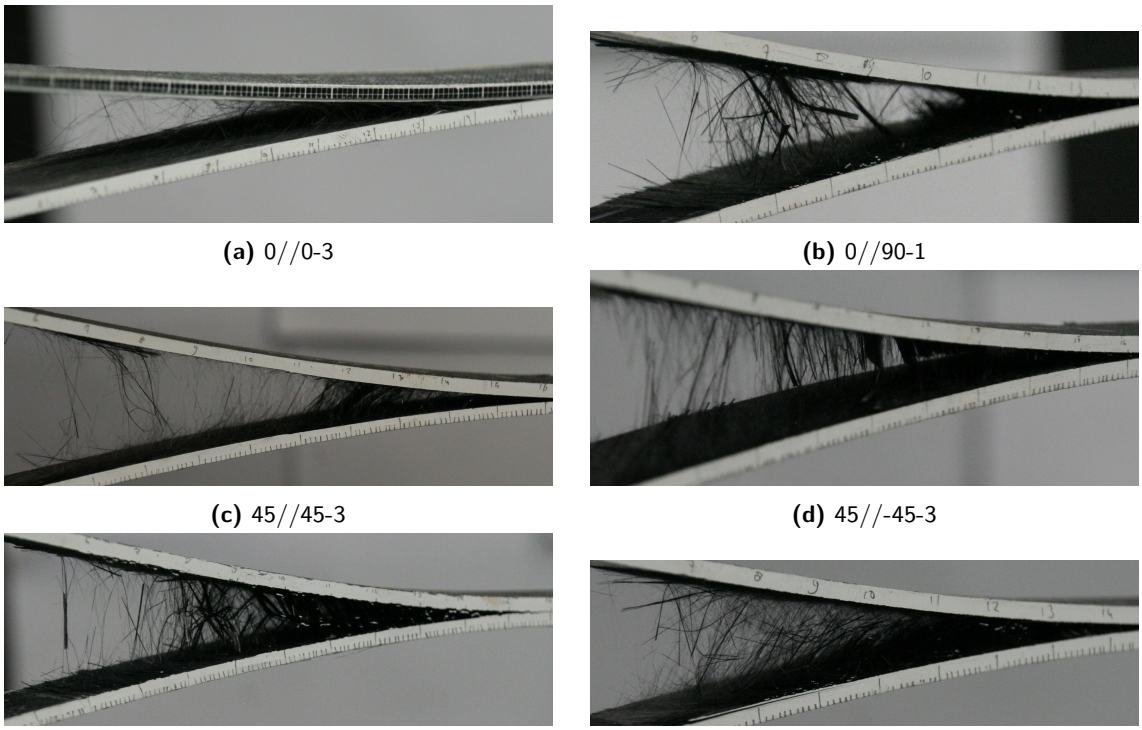

(a) 0//0-3 **(b)** 0//90-1

(c) 45//45-3 **(d)** 45//-45-3

(e) 90//90-1 **(f)** 30//-60-2

Figure 6.6: Pictures of the specimens with increased displacement to see bridging fibres

was to capture whether there were bridging fibres present. These photos of the specimens of which the C-scans are shown in Figure 6.5, can be found in Figure 6.6.

As can be seen in Figure 6.6, fibre bridging occurs in all the layups. Although all the specimens show some fibre bridging, the density varies. Furthermore, the direction of the bridging fibres is different. Although it is hard to see, the fibres obviously bridge in the direction in which they are oriented.

All layups are captured in Figure 6.6, except the 0°//45° interface. This laminate requires additional information. As will be seen in section 6.5, the interface during the manual increment of the test bench deviates from the test's interface. In Figure 6.7a, the fibre bridging is seen after the test. During the test, the crack propagated till the number "10" indicated on the side of the specimen. Hereafter, the crack was manually propagated further. When this crossed "12", the fibre bridging from during the test was visible. Besides the separated bridging fibres, a bunch of fibres with a 45° angle is shown next to each other. Hereafter, the crack propagated through at least one 0° layer. Hence, the resulting fibre bridging in Figure 6.7b is similar to that of a 0°//0° interface. The group of 45° degree fibres are still visible, however, they are no longer connected to both sides.

6.5 Fractography

When the specimens are separated, the fracture surface can be examined. From this, it can be observed through which layers the crack propagated and whether there were any

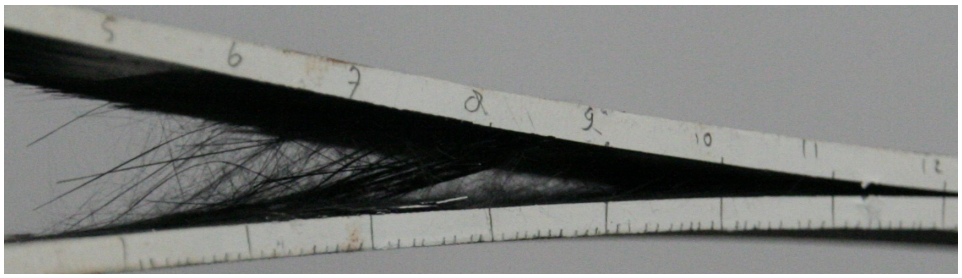

(a) Increased displacement with respect to end of the test

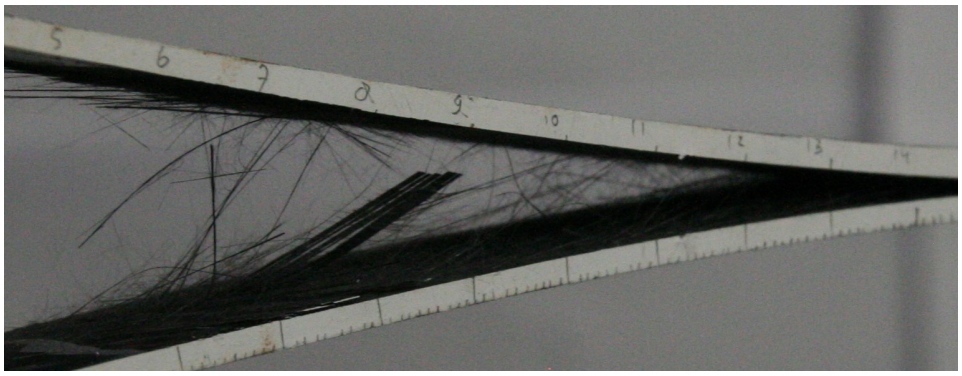

(b) Displacement increased even further

Figure 6.7: Fibre bridging of the 0//45-2 specimens

complications. Images of the disconnected specimens are shown in Figure 6.8. These are the same specimens as examined in section 6.3 and section 6.4. The fracture surfaces of the other specimens can be found in Appendix D.

The specimens were put on a flat white surface. With the use of lamps, the fibres are made to look brighter. The light source causes a reflection on the fibres, and therefore, the fibre direction can be determined. At the top, the specimens have a rectangular shape, marked with a horizontal line, which is the location of the Teflon film. Thus, the crack propagated from top to bottom.

The specimen parts are positioned such that the upper beam is shown on the right-hand side. Subsequently, the part on the left is the lower beam. The right-hand side is simultaneously the representation of the interface. While on the left, its reflected image can be seen. The fibres are visible on either side, whereas their imprints are visible on the opposite side. Therefore, the 45//45-3 and 45//-45-3 specimens appear to be similar. The difference is that, right after the Teflon film, a cross-ply is visible for the 45//-45-3 specimen, but is absent in case of the 45//45-3 specimen. Similarly, in the 30//-60-2 specimen, a cross-ply is visible.

The most remarkable specimen is the 0//45-2 specimen. First, only 45° fibres can be identified. Later on, only 0° fibres are present. A few of these fibres are long and lay loose on the specimen. The 0//90-1 specimen, on the contrary, has primarily 90° fibres where some 0° fibres can be observed through. These 0° fibres are hardly seen in the 90//90-1 specimen.

(a) 0//0-3

(b) 0//45-2

(c) 0//90-1

(d) 45//45-3

(e) 45//-45-3

(f) 90//90-1

(g) 30//-60-2

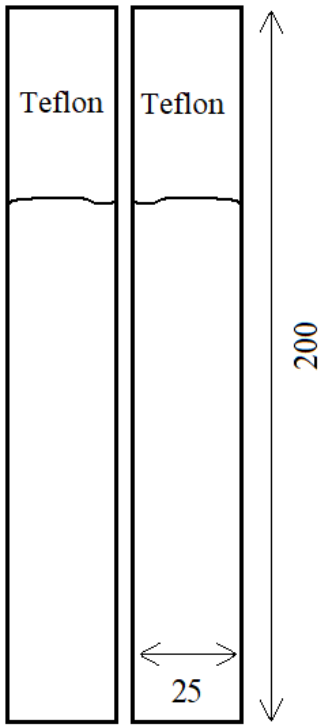

(h) Schematic drawing of the specimen

Figure 6.8: Top view of the specimens' interface after the test

Chapter 7

Discussion

In this chapter, the results of Chapter 6 are discussed. First, the results are compared to prior test. In section 7.2, the influence of the interface angle on delamination resistance is explained. Similarly, the influence of the interface orientation on delamination resistance is discussed in section 7.3. Finally, the influence of the interface on delamination resistance is discussed.

7.1 Comparison with Prior Tests

In this section, the thesis data will be compared with the data produced by Yao [64]. He conducted tests with the same material and parameters, i.e., room temperature fatigue mode I test with R=0.1. These tests were not only conducted with a $0°//0°$ interface, but also the $45°//45°$ and $45°// - 45°$ interfaces. Therefore, it is interesting to see the comparison between his and this research.

In the following sections, resistance curves are presented. Herein, the regression curves of this research's data and the data points of Yao are shown. The same plots without the data of Yao can also be found in Chapter 6 or section C.1. First, in subsection 7.1.1, the data of the $0°//0°$ interfaces is discussed. Second, the $45°//45°$ interfaces are presented in subsection 7.1.2. After that, subsection 7.1.3 discusses the resistance curves of the $45°//-45°$ interfaces. At last, a conclusion is given.

7.1.1 $0°//0°$ Interface

In Figure 7.1, the resistance curves of specimens 0//0-2 and 0//0-3 are shown, together with Sp_7 and Sp_11 of the data set of Yao [64]. For the latter, only two tests are included for each specimen, namely, the first recording and the one with similar increase in precrack as tests 0//0-2.2 and 0//0-3.2. This resulted in the following tests: "Sp_7_1" and "Sp_11_1" for a short precrack and "Sp_7_6" and "Sp_11_5" for the increased precrack. The determined

precrack length is described as "$a-a_0$". Although this differs from the method in this research, the magnitude of the crack growth between the precracks is still the difference between them. A total increase in precrack of 65.44 mm and 56.19 mm for respectively "Sp_7" and "Sp_11" was tested. The precrack lengths of this research's experiments can be found in Table 7.1.

The data points of both the first tests of Yao lay within the two resistance curves of this research. For a similar increase in precrack length however, the data of Yao shows a larger shift to the right. A similar result is also seen in the Thesis of Beyens [29]. Where the steady state of Yao's quasi-static tests was reached earlier and at a higher SERR value. This is explained by the difference in fibre bridging, the tests of Yao showed more fibre bridging. This same increased fibre bridging could also clarify the shift to the right in Figure 7.1. Why the experiments of Yao have more fibre bridging is hard to tell. That the expiration date of the prepreg of this research was already past, might have affected the quality of the laminates. On the other hand, the post-curing in this research has beneficial effects on the degree of curing [70]. Moreover, the toughness of the composite material is increased by the post-curing [71]. All in all, the Sp_7_6 and Sp_11_5 experiments of the research of Yao show an increase in SERR compared to the second tests of this research. There are several reasons why the formation of the bridging fibre differ stated above. However, from this, the quantity of each influence can not be determined with this research.

Table 7.1: Crack lengths of 0°//0° specimens after 100 cycles

Specimen	Crack length (mm)
0//0-2.1	48.399
0//0-2.2	114.322
0//0-3.1	55.38
0//0-3.2	105.503

7.1.2 45°//45° Interface

In Figure 7.2, the resistance curves of specimens with a 45°//45° interface are shown. This means for this research the specimens 45//45-2 and 45//45-3 and specimen 33 of Yao's research [64]. From specimen "Sp_33" this resulted in test 1 and test 4 with names of respectively "Sp_33_1" and "Sp_33_4". The first test of both the researches is to compare this interface without the presence of fibre bridging. Likewise to the 0°//0° interface, the increase of the precrack length is comparable to this research. The difference in precrack length between "Sp_33_1" and "Sp_33_4" is 37.61 mm, whereas the increase in precrack length for the first and second test of this research is 34.354 mm and 28.55 mm for respectively specimens 45//45-2 and 45//45-3, as can be seen in Table 7.2.

Although it looks like tests 45//45-2.1 and 45//45-3.1 differ more than the second tests of the same specimens, the contrary is right due to the logarithmic scale. The minor gridlines between 30 and 300 J/m^2 indicate 30 J/m^2, while from 300 J/m^2 on, they represent 300 J/m^2. Furthermore, as already mentioned in the results, the top data points of both tests 45//45-2.1 and 45//45-3.1, are closer to the top of the regression line indicating the test 45//45-3.1. Therefore, this shows the similarities between the first tests of both researches. Whereas, the regression curve of specimen 45//45-2 is directly shown to coincide with the

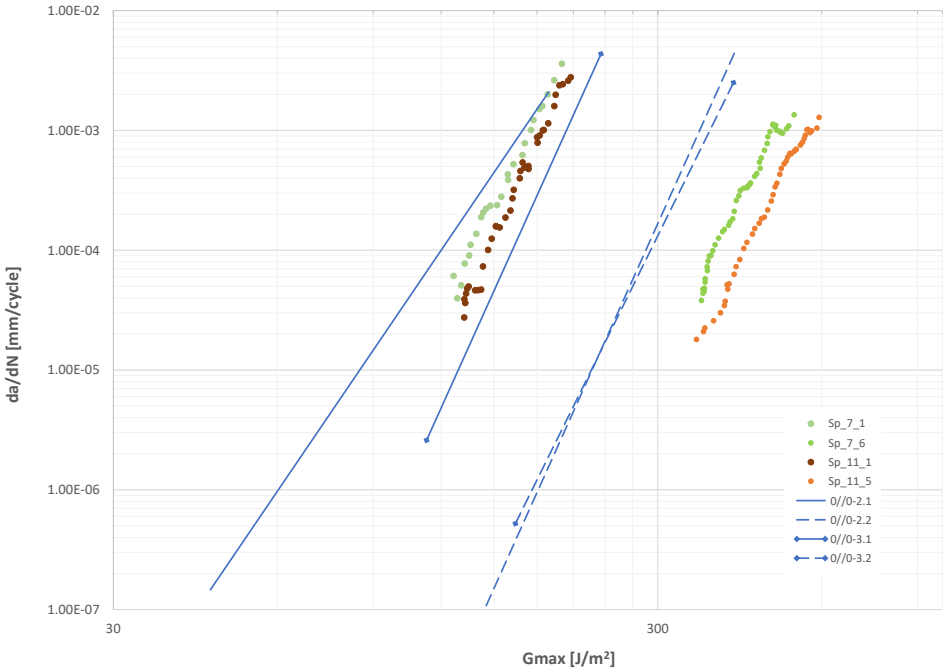

Figure 7.1: da/dN vs Gmax graph of the $0°//0°$ interface including tests performed by Yao [64].

data of experiment Sp_33_4. In total, the data of both researches have similar shifts to the right, given similar increase in precrack lengths.

Table 7.2: Crack lengths of $45°//45°$ specimens after 100 cycles

Specimen	Crack length (mm)
45//45-2.1	44.105
45//45-2.2	78.459
45//45-3.1	45.775
45//45-3.2	74.325

7.1.3 $45°//-45°$ Interface

The data of the test with $45°//-45°$ interfaces is presented in Figure 7.3. Herein, specimens 45//45-2 and 45//45-3 of this research and specimen 53 of Yao's research are shown. From this, a total of four tests are includes. The corresponding precrack lengths are shown in Table 7.3 and Table 7.4 for respectively specimens 45//45-2 and 45//45-3, and specimen 53. With an increase of 9.248 mm, the precrack length increase of specimen 45//45-3 is relatively small. Although tests Sp_53_3 and Sp_53_4 were relatively short, i.e., less than 100,000 cycles, a larger increase in precrack is observed. These tests are included to give a general idea of how it behaves under cyclic loading for that particular precrack length.

The difference between the crack length at the end of the experiment of Sp_53_1 and the crack length at beginning of experiment Sp_53_2 is a negative value. This means that the crack for the second test was reduced with respect to the end of test Sp_53_1. This raises the

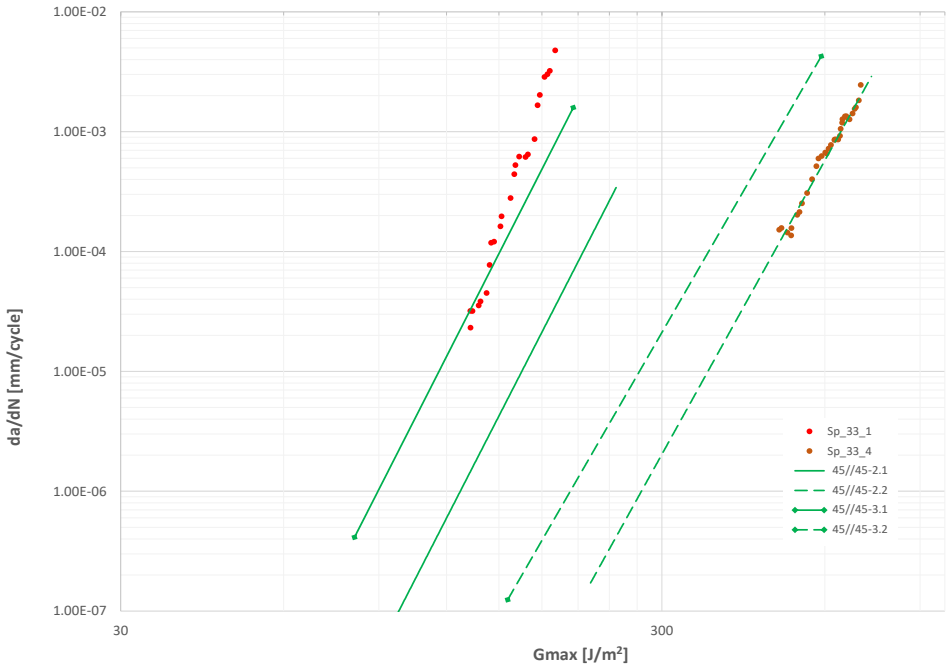

Figure 7.2: da/dN vs Gmax graph of the $45°//45°$ interface including tests performed by Yao [64].

question how reliable these observations of Yao really are. Furthermore, the resistance curves of Yao follow similar curves as this research. However, the steps along these lines should have been smaller, i.e., the fatigue crack growth rate (da/dN) decreases more slowly. Otherwise, it can not be explained how the crack is lengthened longer in the current research's experiments, despite the lesser cycles. The data points of Sp_53_3 goes up and down at the top. This results in maintaining a larger fatigue crack growth rate for a longer period. Moreover, the slope of Sp_53_4 is less steep, which has the same outcome, i.e., a slower decrease in fatigue crack growth rate.

As can be seen in Figure 7.3, the resistance curves of both researches have a change in slope. Furthermore, for both researches, the resistance curves shift to the right with increasing precrack length. In general, the shift to the right is dedicated to fibre bridging [72]. Although fibre bridging for a $45°// - 45°$ interface is visible in section 6.4, a shift from left to right is less distinct than for the other interfaces. All in all, the consistency of the fibre bridging for the 45//-45 interface is diverse. It is hard to predict how the resistance graph would look like. Tests Sp_53_3 and Sp_53_4 demonstrate this unquestionably. With an increase in precrack length, the start of the curve has a shift to the right, but continues with a more gentle slope to cross the previous curve.

Table 7.3: Crack lengths of $45°//-45°$ specimens after 100 cycles

Specimen	Crack length (mm)
45//-45-2.1	58.505
45//-45-2.2	78.459
45//-45-3.1	60.796
45//-45-3.2	70.044

Table 7.4: Crack lengths of Sp_53 from the work of Yao [64]

Specimen	$a - a_0$ (mm)
Sp_53_1	2.054
Sp_53_2	13.188
Sp_53_3	29.459
Sp_53_4	44.394

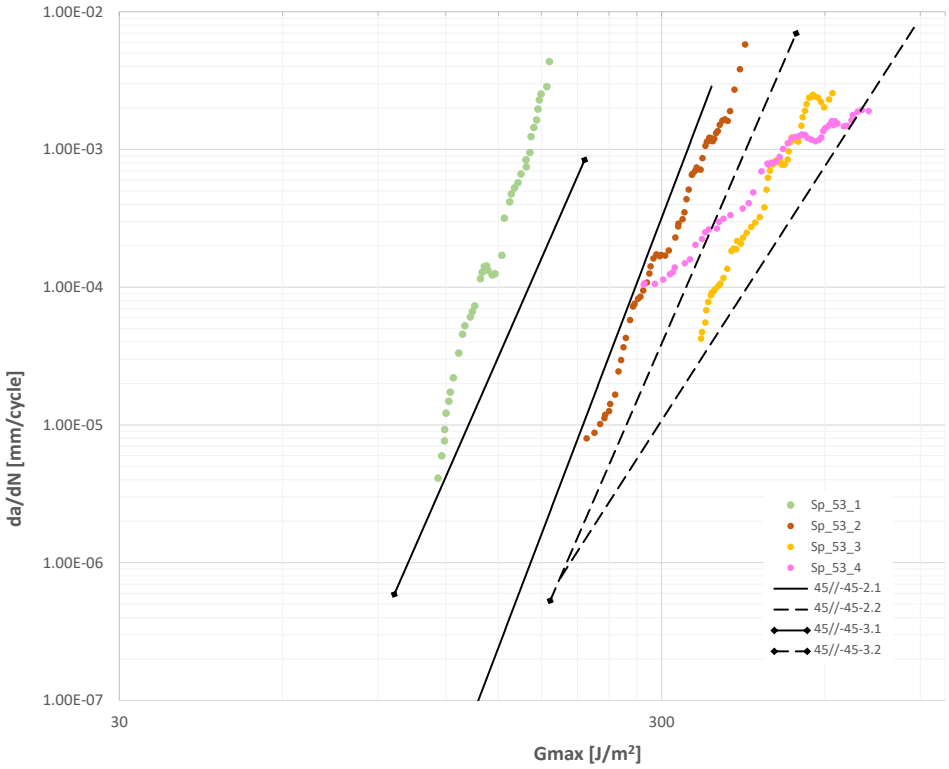

Figure 7.3: da/dN vs Gmax graph of the $45°//-45°$ interface including tests performed by Yao [64].

7.1.4 Conclusion

In conclusion, the experiments of all the different interfaces show a shift to the right with increasing precrack length. Qualitatively, the $0°//0°$ and $45°//45°$ interfaces have more consistent results. A distinct shift to the right is observed when the test started with a longer precrack, whereas the resistance curve of the $45°//-45°$ interface could shift to the right and/or change slope, when the precrack is increased.

The majority of these experiments show similar results except for the second test of the $0°//0°$ interface, where a larger shift to the right of the resistance curve of the research of Yao is observed for similar precrack increase compared to this research. This can be ascribed to the amount of fibre bridging. For the experiments of Yao, the fibre bridging density had increased

to a higher extent. However, whether a steady state is reached can not be determined with these data.

All in all, the results seen in this research correspond to the results of the experiments conducted by Yao. Most of the resistance curves are similar or even coincide. These differences can be designated to scatter of the results. Consequently, the different steps in the manufacturing process as well as the influence of the past expiration date of the prepreg caused minimal changes in the results.

7.2 Influence of the Interface Angle on Delamination Resistance

The fibre bridging in the 0°//0° interface is due to nesting of the fibres during the manufacturing process [40]. When the interface angle is other than 0°, this nesting process is no longer possible. Nevertheless, fibre bridging is observed for 45° and 90° interface angles, see Figure 6.6. Subsequently, an increase in fracture toughness is realised. For these interfaces, the fibre bridging is not caused by nesting, but by oscillating crack propagation. In that way, fibre ligaments are shown in an alternating manner at the fracture surface, as can be seen in Figure 6.8. This repeating change in interface contributes to an even higher fracture toughness than the "conventional" fibre bridging due to nesting, see Figure 6.2. One of the reasons that it is larger, is due to the fact that the zigzag pattern enlarges the "real" crack by 10% [73]. As a result, the value for da/dN will be larger and the magnitude of SERR will probably differ. In case the MCC calculation is still applicable and as the only changing parameter the delamination length is, the SERR value would have been reduced. Furthermore, in nesting, the fibres bridge individually, whereas the other phenomenon corresponds with a bundle of fibres.

The correlation of an increase in interface angle and the increase in fracture toughness can not be made. In Figure 6.2, there is an increase in fracture toughness visible from the 0° to the 45° angle. The 90° angle, however, has comparable, slightly smaller, SERR with similar fatigue crack growth. Furthermore, a small interface angle with respect to the crack propagation would reduce the amount of fibre bridging drastically [74].

The crack of the 0°//45° interfaces propagated through a 0°//45° interface. From the fractography of Figure 6.8b, it becomes clear that, first, the crack propagated (as intended) through the midplane. Later on, the propagation passed to the adjacent 0°//45° interface. The fact that the 0//45 specimens deviated from a single interface, was also observed from pictures that were taken during the test, as can be seen in Figure 7.4. Furthermore, at the fracture surface, 45° fibre ligaments are shown, which indicate a crack propagation that went back and forth between these fibres.

A uniform crack propagation can be seen for the 0°//0° interfaces, see Figure 6.5a. In Figure 6.5, it can be seen that the crack front for both the 0°//45° and 0°//90° interface were less uniform. On the other hand, test 0//45-2.2 shows a difference in crack length between 4 and 5.5 mm, see Table C.1. This, however, is a test where the difference is significantly larger than all other tests with the same interface. This magnitude of difference is more common for the 0°//90° interface, see Table C.2. Additionally, the distribution of the crack length difference for the 0°//90° interface has also a wider spread as the length can differ between

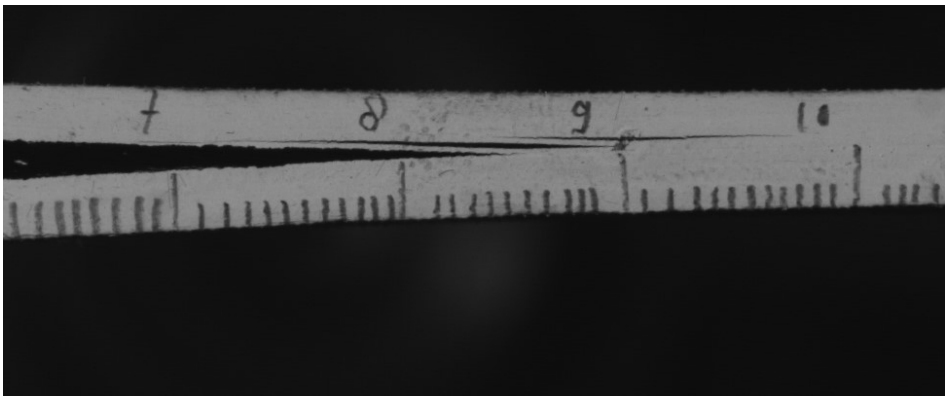

Figure 7.4: Side view of the 0//45-2 specimen during its second test.

2.2 to 6.7 mm for a single test, i.e., test 0//90-2.2. The 0//90-2.1 test even goes over 9 mm in difference, see Table C.2.

7.3 Influence of the Interface Orientation on Delamination Resistance

Just as the influence of the interface angle on delamination resistance, also the influence of the interface orientation on delamination resistance was researched. This was done for two interface angles, i.e., 0° and 90°. First, the 0° angle is discussed in subsection 7.3.1. This is followed by the 90° angle in subsection 7.3.2.

7.3.1 0° Interface Angle

The resistance curves of the interfaces with a 0° angle show an increased shift to the right compared to the 0°//0° interface. Although the magnitude of the shift for the 90°//90° is comparable with the 0°//90° interface, it is less significant for the 45°//45° interface. This had been influenced by the crack propagation interface. As the intentions were that the crack propagated through an interface as the name of the specimen, the reality showed differently. The fractography shows (locally) 45°// − 45° and 0°//90° fracture surfaces for respectively the 45//45 and 90//90 specimens.

The observation of the changes in interface was not limited to the visual aspects of fractography. The C-scans of the 45//45 and 90//90 specimens showed similar results as respectively the 45//-45 and 0//90 specimens, see Figure 6.5. In this case, the interface angle was 90° instead of the wanted 0°. Furthermore, the pictures taken to determine the crack length reveal the zig-zag pattern, as can be seen in Figure 7.5. This was already seen for these interfaces as described by previous research [73] [54]. This, again, indicates a deviation from the aimed interface angle.

The same as for the C-scans, yield for the crack propagation. The difference between crack length of each side was in a similar order of magnitude for the 45//45 and 45//-45 specimens as well as the 90//90 and 0//90 specimens, see section C.2. Moreover, the difference of the

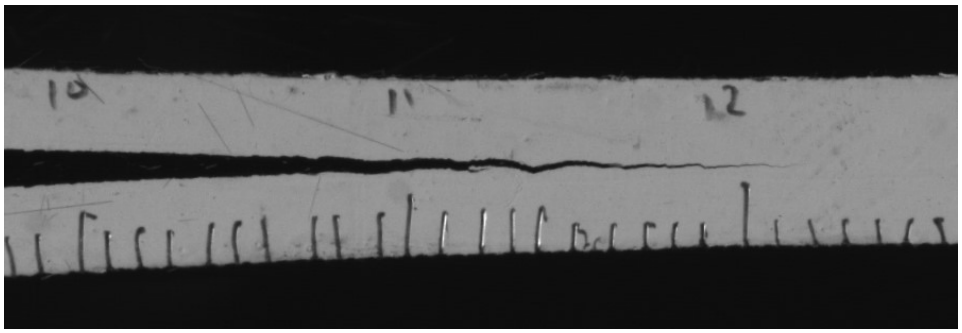

(a) Side view of the 45//45-2 specimen during its second test.

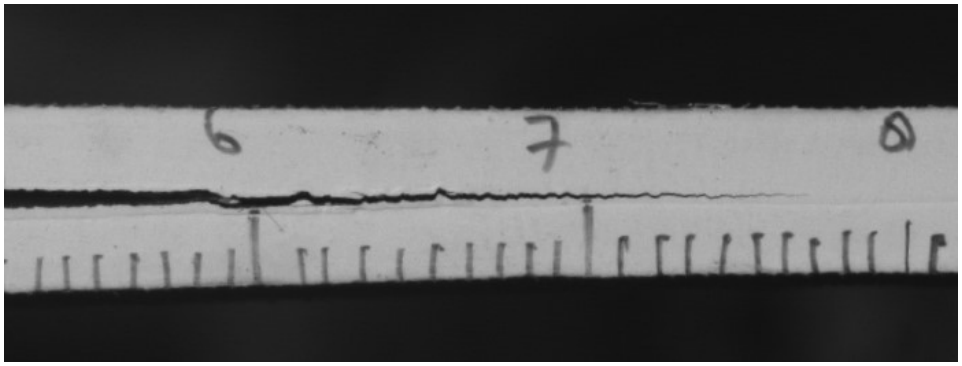

(b) Side view of the 90//90-2 specimen during its first test.

Figure 7.5: Side views of the 45//45-2 and 90//90-2 specimens

crack length for the 90°//90° interface was significantly larger than the 45°//45° interface. This makes that the crack length differences have an ascending magnitude for respectively the 0°//0°, 45°//45° to 90°//90° interface. Nevertheless, the inconsistent difference in crack length of the 90°//90° interface, see Table C.3, it is most likely that for an increase in fibre orientation angle with the same interface angle, the difference in crack length also increases. In order to conclude this, further research with different interfaces is required.

When reviewing the research on specimens with a 0° interface angle, it can be observed that, except for the 0°//0° interface, the crack migrates to an adjacent interface. After some distance, it migrates in the opposite direction. This is a repeating phenomenon, creating a pattern. In this research, the migration was blocked by either a 0° layer or a ply perpendicular to the angle it came from.

7.3.2 90° Interface Angle

The 90° interfaces have similar resistance curves. A clear shift to the right between the different interfaces, as was observed for the different interface angles, can not be distinguished. On the other hand, the C-scans in Figure 6.5 show various crack fronts. The 45°// − 45° interface has a more or less horizontal crack front, whereas the 0°//90° and 30°// − 60° interfaces have a kink in their front. The kink is located where the crack has propagated the least distance. For the 0°//90° interface this kink is approximately in the middle and for 30°// − 60° specimens it is shifted to one of the edges.

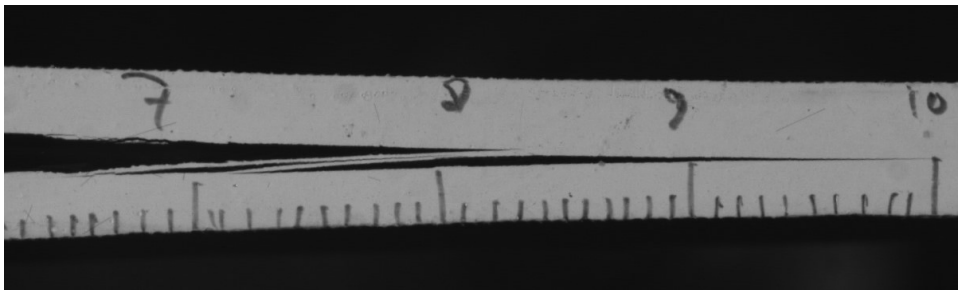

(a) Side view of the 30//-60-1 specimen during its second test.

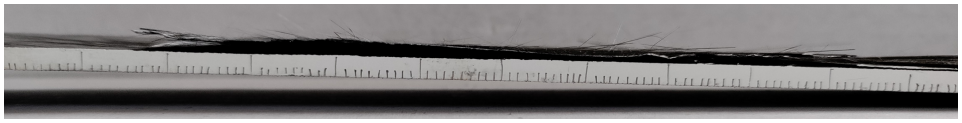

(b) Side view of the 30//-60-1 specimen after the test

Figure 7.6: Side views of the 30//-60-1 specimen during and after the test.

As the kink for the $30°// - 60°$ specimens is not located in the midplane, the crack front has different lengths on either side. This is also observed with the cameras, the differences can be found in section C.2. The difference values of the $30°// - 60°$ specimens are generally larger than for the other specimens with a 90° interface angle, $0°//90°$ and $45°// - 45°$. Furthermore, the more or less horizontal crack front of the $45°// - 45°$ interface results is a relatively low difference in crack length, see Table C.4.

However, in the fractography (Figure 6.8), the $45°//-45°$ and two of the $30°//-60°$ interfaces show similarities, i.e., specimens 30//-60-2 and 30//-60-3. Primarily one layer is shown, the fibre itself on one side and the imprint on the other side. For the $30°//-60°$ specimens, fibres with a $-60°$ angle are better visible than their corresponding cross-ply. On the other hand, specimen 30//-60 shows locally the 0° angle ply as can be seen in Figure D.1g, while the other side shows another crack below the 30° and $-60°$, see Figure 7.6b. During its second test a similar phenomenon was observed as for the 0//45-2 specimen, see Figure 7.6a and Figure 7.4 for respectively the 30//-60-1 and 0//45-2 specimens. This crack migrated on one side to a $0°//30°$ interface and from the other edge to a $60°//0°$ interface. In Figure D.1g, it can be seen that the specimen is separated around the $0°//30°$ interface as the 30° fibres are shown.

Despite having all an interface angle of 90°, the crack propagates differently through the different interfaces. The C-scans of the $0°//90°$ and $30°// - 60°$ interfaces showed a clear kink in the crack front. While, the fracture surface of the $30°//-60°$ and $45°//-45°$ interfaces showed more similarities. Although the differences, their resistance curves lay relatively close to each other.

7.4 Influence of the Interface on Delamination Resistance

Due to testbench limitations, not every experiment was conducted with the same frequency. The second test of most specimens was conducted with a lower frequency than the first one. This, most likely, has affected the results with a higher SERR [55]. The shifts that are seen, however, are increased more significantly than from high frequency fatigue to a lower

frequency fatigue tests.

The specimens in this research had a layup which consisted of the interface complemented with zero degree layers, see Table 4.2. There were, however, two exceptions, the 45//45 and 45//-45 specimens. For comparison with the research of Yao [64], the same layups were used. Consequently, the stiffness in the 0° direction of these specimens was slightly lower compared to the other specimens. The stiffness is increased by thickening the specimens, which, in turn, results in a reduction in the oscillating behaviour of the crack propagation [73]. Therefore, the 45//45 and 45//-45 specimens could have an increase in crack growth resistance when compared to the other specimens as they have a reduced stiffness.

The fibres around the interface were partially pulled out of the specimen, see Figure 6.8. Therefore, one side is still attached to the specimen and on the other side the fibres are loosened. This is seen for all fibres orientations except for the fibres in the 0° direction. For example, specimens with 90° fibres show an alternating pattern. Only one side of the fibre is loosened, while from around the middle axis, it remains connected with the matrix. The side which is loose behaves in a random fashion.

The interfaces with the same fibre orientation have nested fibres. For a 0°//0° delamination plane, this results in fibre bridging. On the other hand, fibres with a higher orientation angle still nest into the fibres of the same orientation in the adjacent layer(s), but prevent the crack from propagating through. Hence, the crack migrates to an adjacent interface, where it can propagate. This behaviour leads to a the zig-zag crack propagation pattern [73] [54] and thus a higher fracture resistance.

The specimens with an asymmetric layup showed an asymmetric crack front in the C-scan, see Figure 6.5. The crack front tends to "follow" the fibres of either of the fibre directions around the interface. This is caused due to a combination of the fibre direction and the asymmetry of the specimens. The coupling through the asymmetries causes a change in skewness and the curvature of the G distribution [34] [36]. Accordingly, the crack front is shaped differently than for the "common" 0°//0° interfaces. Furthermore, the coupling introduces additional failure modes to the specimen, i.e. it is no longer purely mode I delamination [73]. However, the B_t and D_c values are lower than the threshold values proposed in earlier research [34] [36]. Hence, the additional induced failure modes are minimal.

Differences in crack length between the different sides of the specimen are also seen in symmetrical layups, see section C.2. Accordingly, the C-scan in Figure 6.5 showed an incline compared to a perpendicular front. During the experiments this difference changed for several specimens, see for example Table C.3. Hence, the crack propagation along the width is not constant. Not only changes it from side to side, but the C-scans showed also a non-uniform crack front. Whereas for a 0°//0° interface, the edges show a slight reduced crack growth, for specimens with at least one 90° layer in the interface, the middle shows a decrease in crack length.

7.5 Conclusion

Different interfaces affect the results of fibre bridging and thus also the fatigue delamination growth rate. Although the crack propagation occurred in an unintended manner, bridging fibres were observed, which indicate that the crack propagated through more than just a single

interface. Some cracks migrated from the interface (as the specimen's name) to an adjacent delamination plane. As a result, the resistance curves of these specimens do not represent the intended interface, but the result of a specimen with the adjacent interface. Furthermore, some cracks propagated around the fibres of a single ply. Subsequently, the interface went form $0//\alpha$ to $\alpha//0$ or vice versa. As the crack only propagated through the interface locally and merely as a migration to another plane, the resistance curves show the crack migration behaviour instead of the interface propagation.

All in all, this research brings additional knowledge to the field of fatigue delamination growth. Based on past research, this research is a good extension of the fatigue delamination growth. Wherein the past research is limited in the use of MD specimens, the present research shows the occurrence of fibre bridging for multiple interfaces. The origin of these bridging fibre varies from nesting to an oscillatory pattern between adjacent layers. From which the last, show an increase in fracture resistance.

Chapter 8

Conclusion and Recommendations

In this chapter, the conclusion of this research is given. After that, recommendations for further research are suggested.

8.1 Conclusion

This research aimed for a better understanding of fatigue Mode I delamination at MD interfaces. This led to the following research question: "*What is the influence of the fibre orientation at the interface on delamination growth rate under cyclic loading?*" To answer this question, it was separated into the influence of the angle between the fibres around the interface, and the influence of the orientation of this angle.

For all the specimens, fibre bridging is observed, i.e., all tested fibre orientations show bridging fibres. This was shown with an increased delamination resistance for a longer precrack. The magnitude of which is dominated by the amount of fibre bridging. More fibre bridging results in a better delamination resistance. Hence, all the first resistance curves were located to the left of the second curves, indicating an increase in fibre bridging. Whether a steady state was reached or if it keeps increasing, however, can not be concluded with this research.

Furthermore, not all bridging fibres had the same origin. Interfaces with the fibre orientation longitudinal to the crack propagation were nested in the adjacent layers during the manufacturing process, whereas, the crack propagation perpendicular to the fibres showed oscillating delamination behaviour. The latter also showed a more significant increase in the fatigue delamination growth resistance for similar precrack increases.

In the results, from the C-scan, it was found that the specimens had dissimilar crack fronts. It was already known that it was caused by coupling effect of the asymmetrical layups. As the crack front tends to propagate towards the direction of the fibres of either of the fibre orientations around the interface, this also has an influence.

All in all, it can be concluded that there is an influence of the fibre orientation. However, the interface angle and the interface on their own are unrelated to the amount of fibre bridging.

The fibre bridging density and how the fibres will bridge is determined by the combination of both the interface angle and the interface orientation. It affects besides the density of the fibre bridging also the crack fronts and, consequently, the fracture surface.

8.2 Recommendations

For future research on the topic of fatigue delamination growth, one should keep in mind that in order to compare the results in the best way possible, all parameters should be identical. The frequency and the precrack length should be kept the same for every test. Ideally, multiple tests are performed on a single specimen to show the increase or steady state of the fibre bridging. Furthermore, the layup of each specimen should aim for similar stiffness (in all directions).

Second, it is recommended that the use of non $0°//0°$ interfaces should be extended. Other interfaces show also fibre bridging and these have a large influence on the fracture resistance. The origin of these bridging fibres is different i.e., not nesting, and thus requires a more detailed examination. Similarly, the focus should lie on non zero degree interface angles. The crack propagation of these zero degree interface angles migrate (mostly) to an adjacent delamination plane and is only temporary within the intended plies.

Third, as the zig-zag pattern increases the fracture resistance, the tests of a $0°//0°$ interface are conservative. In order to make sure a construction with MD laminates is strong enough, its design should at least withhold the mode I delamination of a $0°//0°$ interface. In this way, money and time can be saved by preventing testing every possible interface.

Furthermore, it would be interesting to see what happens when the width of the specimen is enlarged. This could have an influence on the fibre bridging behaviour of MD specimens. The region where the fibre is still connected with the matrix material might increase. Moreover, the fibre can be pulled out of the material for a longer distance. Subsequently, the fracture resistance will increase. It is good to investigate whether the same effects happen in a specimen with 90 degree orientated fibres around the interface.

Last, further research is needed to show which region on the interface angles generates which type of fibre bridging, e.g., due to nesting or a zig-zag pattern. Depending on the application, it might be interesting to have certain angles, which have or may not have fibre bridging. With more insights of how and when it happens, a less conservative design can be made possible.

References

[1] Mrazova Maria. Advanced composite materials of the future in aerospace industry. *INCAS BULLETIN*, 5(3):139–150, 2013. The Faculty of Operation and Economics of Transport, The Air Transport Department Univerzitna 1, 010 26 Zilina, Slovak Republic.

[2] Justin Hale. *Boeing 787 from the Ground Up.* The Boeing Company, 2008.

[3] Lucas Amaral, Liaojun Yao, René Alderliesten, and Rinze Benedictus. The relation between the strain energy release in fatigue and quasi-static crack growth. *Engineering Fracture Mechanics*, 145:86–97, 2015.

[4] Rick Domingo. *AC 43-4B - Corrosion Control for Aircraft.* Federal Aviation Administration, 2018.

[5] C. Bathias. The fatigue of high performance composite materials. In C. Moura Branco and L. Guerra Rosa, editors, *Advances in Fatigue Science and Technology*, pages 659–676. Springer Netherlands, 1989.

[6] Golam Newaz. Damage tolerance analysis for advanced composites. In *Wiley Encyclopedia of Composites.* John Wiley & Sons, Inc., 2012.

[7] L. Amaral. *Towards fundamental understanding of interlaminar ply delamination growth under mode II and mixed-mode loading.* PhD thesis. Delft University of Technology, 2018.

[8] M. R. Wisnom. The role of delamination in failure of fibre-reinforced composites. *Philosophical Transactions of the Royal Society A: Mathematical, Physical and Engineering Sciences*, 370(1965):1850–1870, 2012.

[9] Alan Arnold Griffith. The phenomena of rupture and flow in solids. *Royal Society*, 221(582), 1921.

[10] Nestor Perez. *Fracture Mechanics.* Springer International Publishing Switzerland, second edition, 2017.

[11] ASTM D5528-13. Standard test method for mode I interlaminar fracture toughness of unidirectional fiber-reinforced polymer matrix composites, 2013.

[12] J.A. Pascoe. *Characterisation of Fatigue Crack Growth in Adhesive Bonds*. PhD thesis. Delft University of Technology, 2016.

[13] G. R. Irwin. *Fracture dynamics*. American Society for Metals, 1948.

[14] E. Orowan. Fracture and strength of solids. *Reports on Progress in Physics*, 12(1):185–232, 1949. Publisher: IOP Publishing.

[15] Michael Janssen, Jan Zuidema, and Russell Wanhill. *Fracture Mechanics*. Spon Press, second edition edition, 2002.

[16] S.T. Rolfe and J.M. Barsom. *Fracture and Fatigue Control in Structures: Applications of Fracture Mechanics*. Prentice-Hall civil engineering and engineering mechanics series. Prentice-Hall, 1977.

[17] G. R. Irwin. Analysis of stresses and strains near the end of a crack traversing a plate. *Journal of Applied Mechanics*, 24:361–364, 1957.

[18] G. R. Irwin. *Fracture Mechanics*. Proceedings of the First Symposium on Naval Structural Mechanics. 1958.

[19] Paul C Paris, M Gomez, and W Anderson. A rational analytic theory of fatigue. *Trend Engineering*, 13:9–14, 1961.

[20] P. Paris and F. Erdogan. A critical analysis of crack propagation laws. *Journal of Basic Engineering*, 85(4):528–533, 1963.

[21] Paul C Paris. The fracture mechanics approach to fatigue. *Sagamore army materials research conference*, 10:107–132, 1964.

[22] William Clark. Fracture mechanics in fatigue. *Experimental Mechanics*, 11:421–428, 1971.

[23] J.A. Pascoe, R.C. Alderliesten, and R. Benedictus. Methods for the prediction of fatigue delamination growth in composites and adhesive bonds – a critical review. *Engineering Fracture Mechanics*, 112-113:72–96, 2013.

[24] Calvin Rans. Misinterpreting the results: How similitude can improve our understanding of fatigue delamination growth. *Composites Science and Technology*, 2011.

[25] C D Rans and R C Alderliesten. Formulating an effective strain energy release rate for a linear elastic fracture mechanics description of delamination growth. 2014.

[26] Roman Růžek, Martin Kadlec, and Lucie Petrusová. Effect of fatigue loading rate on lifespan and temperature of tailored blank C/PPS thermoplastic composite. *International Journal of Fatigue*, 113:253–263, 2018.

[27] Ramesh Talreja. Fatigue of composite materials. In Holm Altenbach and Wilfried Becker, editors, *Modern Trends in Composite Laminates Mechanics*, pages 281–294. Springer Vienna, 2003.

[28] J Justo, J. C. Marin, F Paris, and J Cañas. The effect of frequency on fatigue behaviour of graphite-epoxy composites. volume 16, 2014.

[29] M Beyens. *Effect of Ambient Temperature on Fatigue Delamination Growth in Composite Laminates*. Msc Thesis. Delft University of Technology, 2021.

[30] ASTM D6115-97. Standard test method for mode i fatigue delamination growth onset of unidirectional fiber-reinforced polymer matrix composites, 2019.

[31] J.A. Pascoe, R.C. Alderliesten, and R. Benedictus. On the physical interpretation of the r-ratio effect and the LEFM parameters used for fatigue crack growth in adhesive bonds. *International Journal of Fatigue*, 97:162–176, 2017.

[32] R.C. Alderliesten. Critical review on the assessment of fatigue and fracture in composite materials and structures. *Engineering Failure Analysis*, 35:370–379, 2013.

[33] D Wilkins, J Eisenmann, R Camin, W Margolis, and R Benson. Characterizing delamination growth in graphite-epoxy. In K Reifsnider, editor, *Damage in Composite Materials: Basic Mechanisms, Accumulation, Tolerance, and Characterization*, pages 168–168–16. ASTM International, 1982.

[34] B D Davidson, R Krüger, and M König. Three-dimensional analysis of center delaminated unidirectional and multidirectional single-leg bending specimens. *Composites Science and Technology*, 54:385–394, 1995.

[35] J.A. Pascoe, N. Zavatta, E. Troiani, and R.C. Alderliesten. The effect of bond-line thickness on fatigue crack growth rate in adhesively bonded joints. *Engineering Fracture Mechanics*, 229:106959, 2020.

[36] C.T. Sun and S. Zheng. Delamination characteristics of double-cantilever beam and end-notched flexure composite specimens. *Composites Science and Technology*, 56(4):451–459, 1996.

[37] W Johnson, J Masters, T O'Brien, J Reeder, and J Crews. Redesign of the mixed-mode bending delamination test to reduce nonlinear effects. *Journal of Composites Technology and Research*, 14(1), 1992.

[38] JR Reeder. A criterion to control nonlinear error in the mixed-mode bending test. In CE Bakis, editor, *Composite Materials: Testing and Design, Fourteenth Volume*, pages 349–371. ASTM International, 2003.

[39] ASTM D6671/D6671M-19. Test method for mixed mode I-mode II interlaminar fracture toughness of unidirectional fiber reinforced polymer matrix composites.

[40] WS Johnson and PD Mangalgiri. Investigation of fiber bridging in double cantilever beam specimens. *Journal of Composites, Technology and Research*, 9(1):10–13, 1987. Place: West Conshohocken, PA Publisher: ASTM International.

[41] Rafiullah Khan. *Delamination growth in composites under fatigue loading.* PhD thesis. Delft University of Technology, 2013. ISBN: 9789088917158 OCLC: 905870430.

[42] Rafiullah Khan. Fiber bridging in composite laminates: A literature review. *Composite Structures*, 229:1–15, 2019.

[43] A.P. Mouritz, M.K. Bannister, P.J. Falzon, and K.H. Leong. Review of applications for advanced three-dimensional fibre textile composites. *Composites Part A: Applied Science and Manufacturing*, 30(12):1445–1461, 1999.

[44] A.P. Mouritz. Review of z-pinned composite laminates. *Composites Part A: Applied Science and Manufacturing*, 38(12):2383–2397, 2007.

[45] Liaojun Yao, R.C. Alderliesten, and R. Benedictus. The effect of fibre bridging on the paris relation for mode i fatigue delamination growth in composites. *Composite Structures*, 140:125–135, 2016.

[46] Rafiullah Khan, René Alderliesten, Liaojun Yao, and Rinze Benedictus. Crack closure and fibre bridging during delamination growth in carbon fibre/epoxy laminates under mode I fatigue loading. *Composites Part A: Applied Science and Manufacturing*, 67:201–211, 2014.

[47] Larissa Sorensen, John Botsis, Thomas Gmür, and Joël Cugnoni. Delamination detection in CFRP laminated with embedded small-diameter fiber bragg grating sensors. *Composites Part A: Applied Science and Manufacturing*, pages 87–96, 2007.

[48] Liaojun Yao, Yi Sun, R.C. Alderliesten, R. Benedictus, and Meiying Zhao. Fibre bridging effect on the paris relation for mode I fatigue delamination growth in composites with consideration of interface configuration. *Composite Structures*, 159:471–478, 2017.

[49] Xiao-Zhi Hu and Yiu-Wing Mai. Mode I delamination and fibre bridging in carbon-fibre/epoxy composites with and without pval coating. *Composites Science and Technology*, 46:147–156, 1993.

[50] Emile Smith Greenhaigh. *Characterisation of mixed-mode delamination growth in carbon-fibre composites*. Imperial College London, 1998.

[51] D.J. Nicholls and J.P. Gallagher. Determination of GIC in angle ply composites using a cantilever beam test method. *Journal of Reinforced Plastics and Composites*, 2(1):2–17, 1983. Publisher: SAGE Publications Ltd STM.

[52] Y. Sun, L. Yao, R. C. Alderliesten, and R. Benedictus. Mode I quasi-static delamination growth in multidirectional composite laminates with different thicknesses. In *Proceedings of the American Society for Composites - 31st Technical Conference, ASC 2016*, 2016.

[53] Simon Baril-Gosselin, , and Chun Ping Li. Characterizing and predicting the effects of weave geometry on mode I fracture toughness of composites. In *American Society for Composites 31st Annual Technical Conference and Proceedings*, 2016.

[54] D. Mollenhauer, S. Baril-Gosselin, E. Iarve, L. Chun, D. Rapking, E. Zhou, and M. Braginsky. Mode I fracture specimens exhibiting oscillatory crack migration. In *ECCM18 - 18th European Conference on Composite Materials*, 2018.

[55] Liaojun Yao, René Alderliesten, Meiying Zhao, and Rinze Benedictus. Bridging effect on mode I fatigue delamination behavior in composite laminates. *Composites Part A: Applied Science and Manufacturing*, 63:103–109, 2014.

[56] S Stutz. Studies of mode I delamination in monotonic and fatigue loading using FBG wavelength multiplexing and numerical analysis. *Composites Science and Technology*, pages 443–449, 2011.

[57] Chaim Ishbir, Leslie Banks-Sills, Victor Fourman, and Rami Eliasi. Delamination propagation in a multi-directional woven composite DCB specimen subjected to fatigue loading. *Part B*, pages 180–189, 2014.

[58] Ido Simon. Mode I delamination propagation and R-ratio effects in woven composite DCB specimens for a multi-directional layup. *International Journal of Fatigue*, page 15, 2017.

[59] Leslie Banks-Sills, Ido Simon, and Tomer Chocron. Multi-directional composite laminates: fatigue delamination propagation in mode I—a comparison. *International Journal of Fracture*, 219(2):175–185, 2019.

[60] T. Chocron and L. Banks-Sills. Nearly mode I fracture toughness and fatigue delamination propagation in a multidirectional laminate fabricated by a wet-layup. *Physical Mesomechanics*, 22(2):107–140, 2019.

[61] Mor Mega, Orly Dolev, and Leslie Banks-Sills. Two- and three-dimensional failure criteria for laminate composites. *Journal of Applied Mechanics*, 87:1–18, 2019.

[62] Liaojun Yao, Yi Sun, Licheng Guo, Xiuqi Lyu, Meiying Zhao, Liyong Jia, R.C. Alderliesten, and R. Benedictus. Mode I fatigue delamination growth with fibre bridging in multidirectional composite laminates. *Engineering Fracture Mechanics*, 189:221–231, 2018.

[63] Z. Daneshjoo, M.M. Shokrieh, and M. Fakoor. A micromechanical model for prediction of mixed mode i/II delamination of laminated composites considering fiber bridging effects. *Theoretical and Applied Fracture Mechanics*, 94:46–56, 2018.

[64] Rene Alderliesten and L. (Liaojun) Yao. *Database: Mode I fatigue delamination growth in composite laminates with fibre bridging.* Delft University of Technology, Dec 2017.

[65] Delta tech. DT120 versatile high toughness epoxy matrix. *Technical data sheet*, Issue 10, February 2015.

[66] Goodfellow. Polytetrafluoroethylene-film. *Technical data sheet*, Product Code: FP30-FM-000100.

[67] 3M. 3M Scotch-Weld epoxy adhesive EC-2216 b/a. *Technical data sheet*, June 2009.

[68] R.C. Alderliesten and A.J. Brunner. Determination of mode I fatigue delamination propagation in unidirectional fibre-reinforced polymer composites. *Test protocol*, Version 3.2, 2019-2020.

[69] ASTM E647-00. Standard test method for measurement of fatigue crack growth rates. *ASTM Test protocol*, 03.01:43, 2017.

[70] Ping Hu, Ditho Pulungan, Ran Tao, and Gilles Lubineau. Influence of curing processes on the development of fiber bridging during delamination in composite laminates. *Composites Part A: Applied Science and Manufacturing*, 149, 07 2021.

[71] R Tucker, P Compston, and P.-Y.B Jar. The effect of post-cure duration on the mode I interlaminar fracture toughness of glass-fibre reinforced vinylester. *Composites Part A: Applied Science and Manufacturing*, 32(1):129–134, 2001.

[72] L Yao. Mode I fatigue delamination growth in composite laminates with fibre bridging. 12 2015.

[73] Liaojun Yao, Hao Cui, Yi Sun, Licheng Guo, Xiangming Chen, Meiying Zhao, and R. C. Alderliesten. Fibre-bridged fatigue delamination in multidirectional composite laminates. *Composites Part A: Applied Science and Manufacturing*, 115:175–186, April 2018.

[74] L Asp, A Sjögren, and E Greenhalgh. Delamination growth and thresholds in a carbon/epoxy composite under fatigue loading. *Journal of Composites Technology Research*, 23(2):55–68, April 2001.

Appendix A

Appendix A: C-Scan

In this Appendix the images of the performed C-scans are shown. First, in section A.1, C-scans are shown after curing to see whether there were imperfections. Second, after the tests the crack front was visualised with a C-scan in section A.2.

A.1 Laminates after Autoclave Curing

A.2 Specimens after Testing

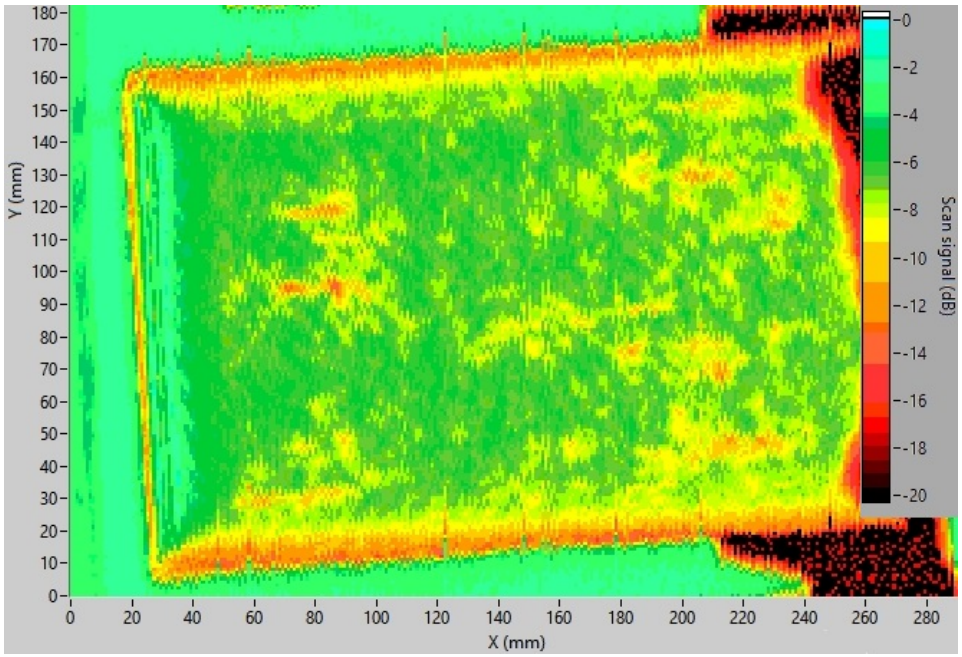

(a) C-scan of the 0//0 laminate. Note: the dimensions on the X and Y axis are not to scale.

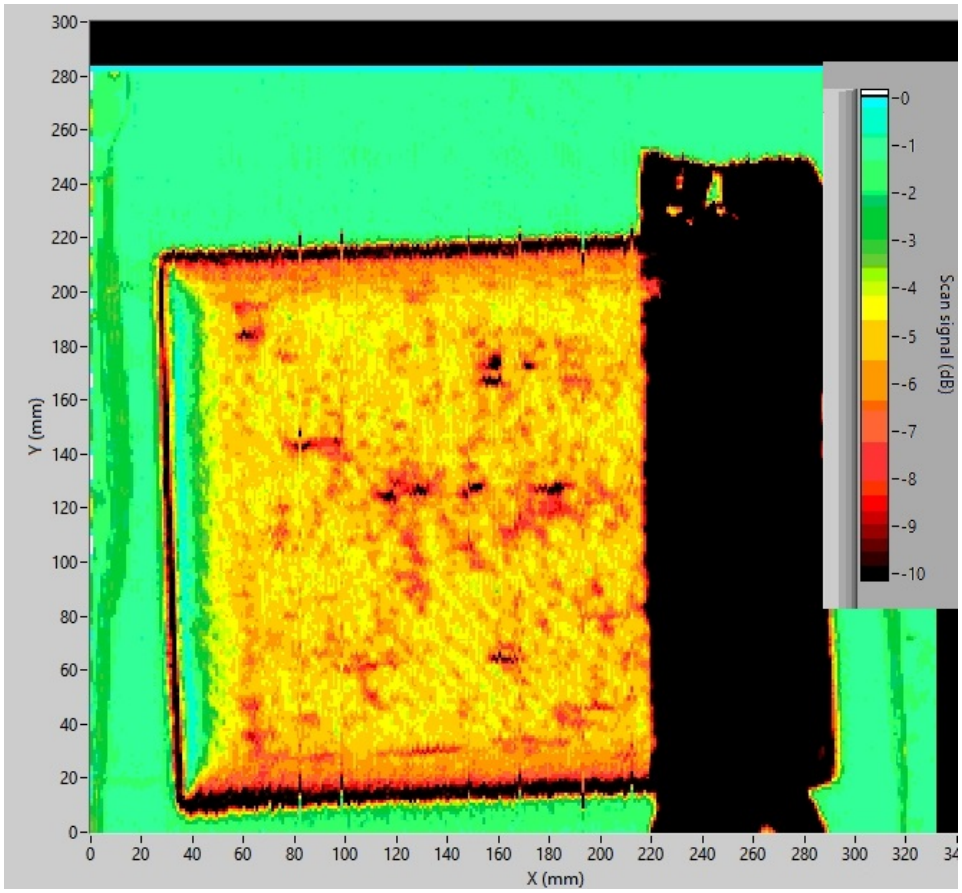

(b) C-scan of the 0//45 laminate. Note: the dimensions on the X and Y axis are not to scale.

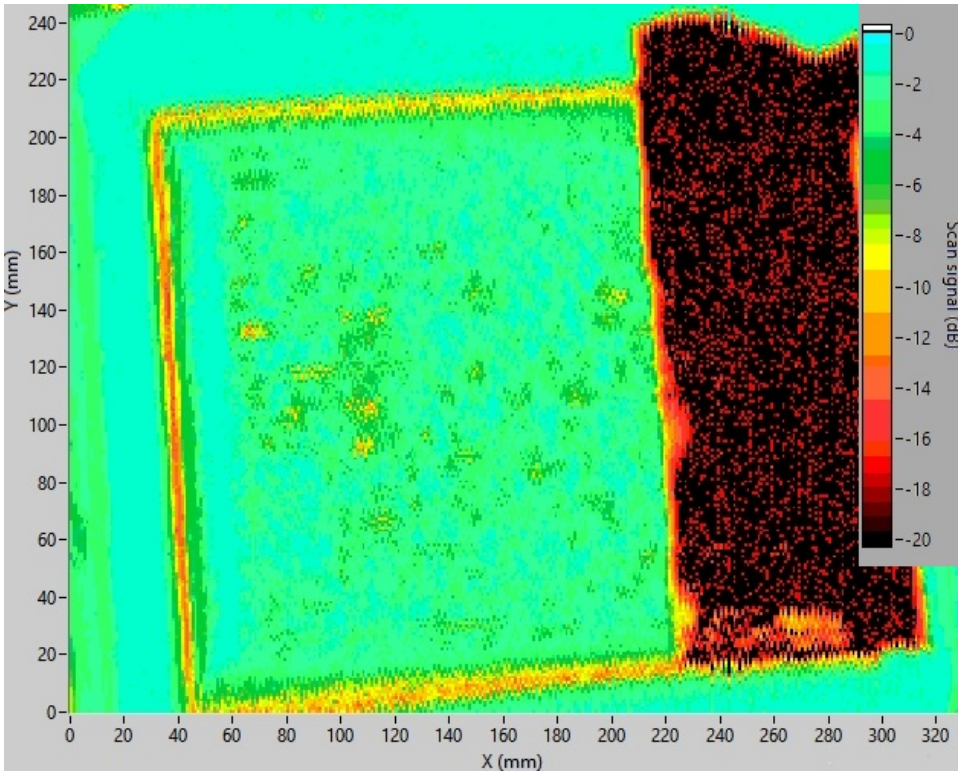

(c) C-scan of the 0//90 laminate. Note: the dimensions on the X and Y axis are not to scale.

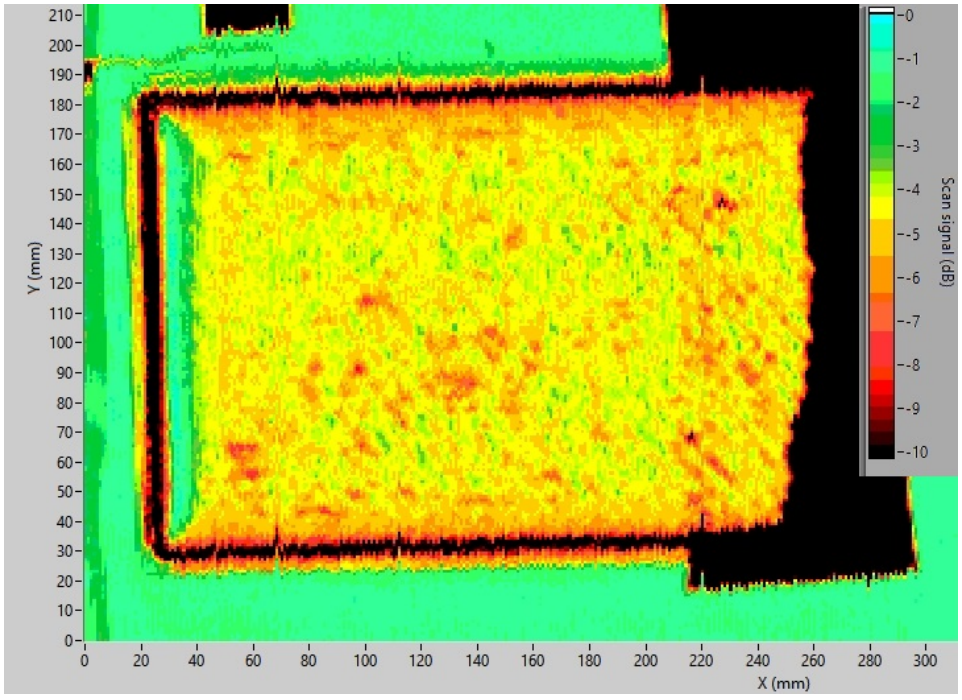

(d) C-scan of the 45//45 laminate. Note: the dimensions on the X and Y axis are not to scale.

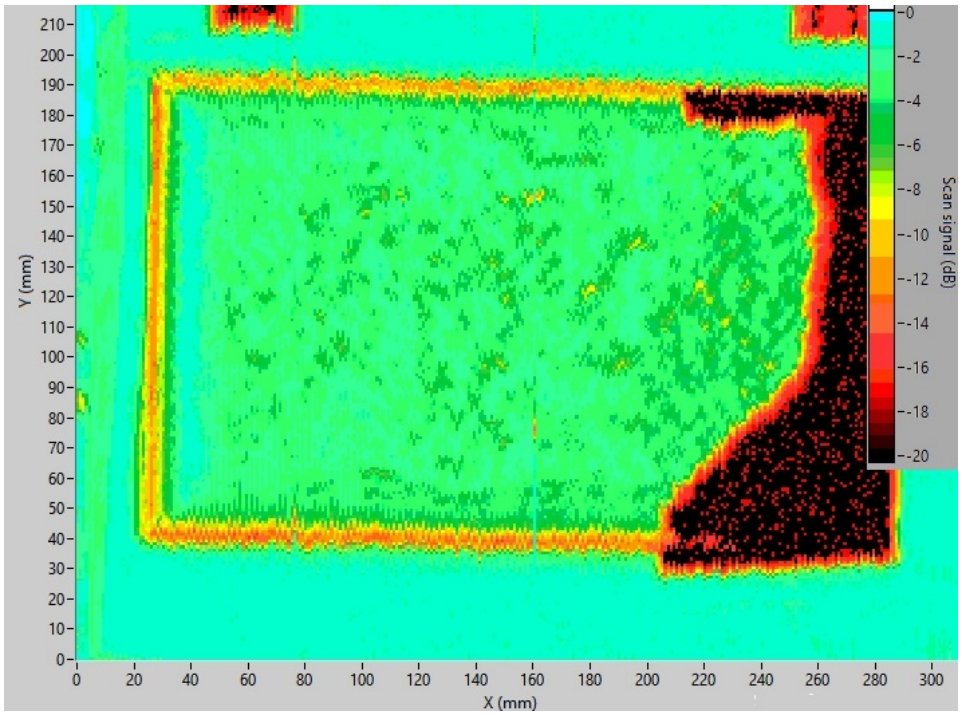

(e) C-scan of the 45//-45 laminate. Note: the dimensions on the X and Y axis are not to scale.

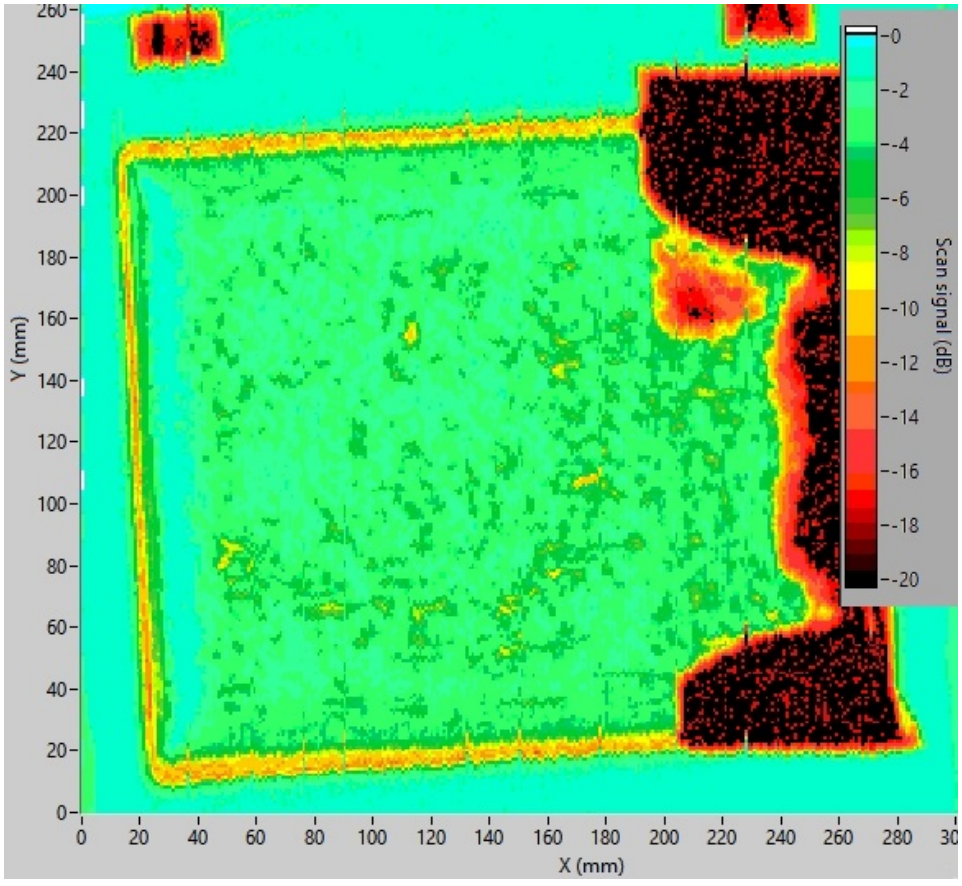

(f) C-scan of the 90//90 laminate. Note: the dimensions on the X and Y axis are not to scale.

Figure A.1: C-scans of the specimens after the curing

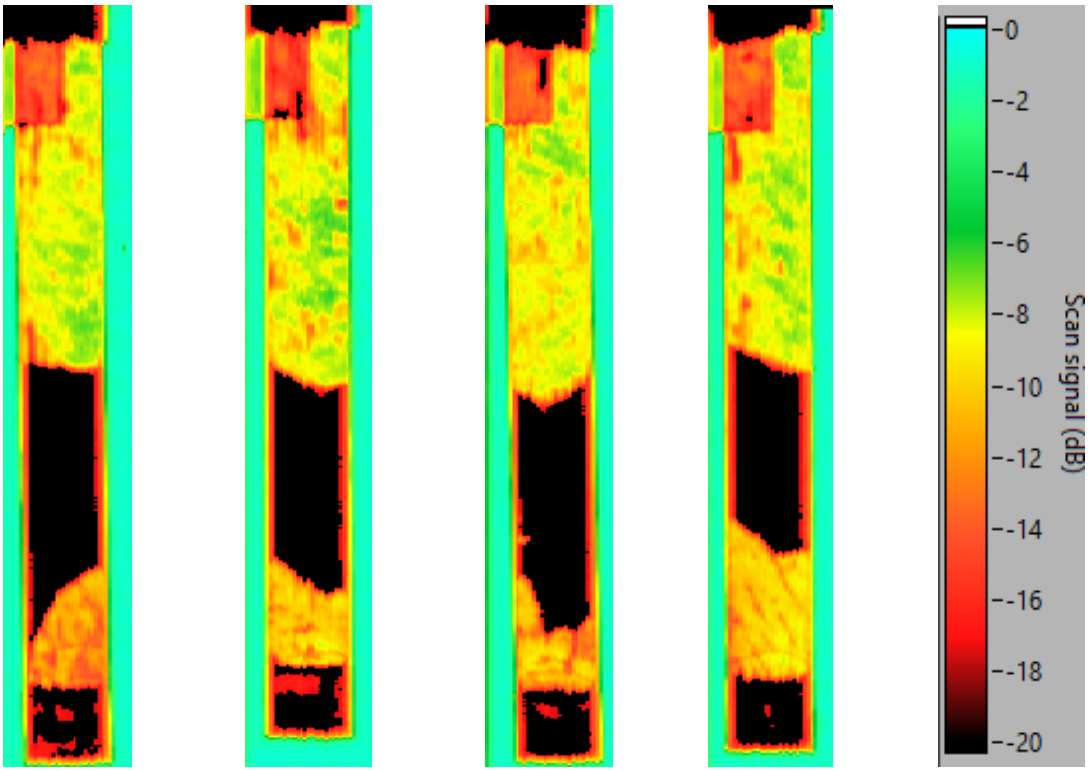

(a) 0//45-1 **(b)** 0//90-3 **(c)** 90//90-2 **(d)** 30//-60-1 **(e)** C-scan legend

Figure A.2: C-scans of the specimens after the test

Appendix B

Appendix B: Test Overview

In this Appendix a list of all the conducted experiments in this research project can be found in Table B.1. This include the frequency, total number of cycles and the pre-crack length after 100 cycles.

Table B.1: List of conducted tests

Test	Specimen	Frequency [Hz]	Total cycles	Pre-crack length [mm] (After 100 cycles)
0//0-2.1	0//0-2	5	288000	48.399
0//0-2.2	0//0-2	2	359000	114.322
0//0-3.1	0//0-3	5	279000	55.38
0//0-3.2	0//0-3	2.5	195000	105.503
45//45-2.1	45//45-2	5	439000	44.105
45//45-2.2	45//45-2	2	351000	78.459
45//45-3.1	45//45-3	5	133000	45.775
45//45-3.2	45//45-3	2.5	559000	74.325
90//90-1.1	90//90-1	5	155000	55.745
90//90-1.2	90//90-1	2	322000	97.261
90//90-2.1	90//90-2	5	149000	57.542
90//90-2.2	90//90-2	3	152000	76.746
0//45-1.1	0//45-1	5	155000	48.273
0//45-1.2	0//45-1	4	201000	76.947
0//45-2.1	0//45-2	5	155000	49.062
0//45-2.2	0//45-2	4	198000	72.401
0//90-1.1	0//90-1	5	154000	54.269
0//90-1.2	0//90-1	3	211000	84.21
0//90-3.1	0//90-3	5	156000	53.761
0//90-3.2	0//90-3	5	254000	72.468
45//-45-2.1	45//-45-2	5	432000	58.505
45//-45-2.2	45//-45-2	2	451000	78.459
45//-45-3.1	45//-45-3	5	150000	60.796
45//-45-3.2	45//-45-3	4	201000	70.044
30//-60-1.1	30//-60-1	5	160000	-
30//-60-1.2	30//-60-1	4	201000	73.055
30//-60-2.1	30//-60-2	5	153000	55.642
30//-60-2.2	30//-60-2	4	206000	73.254
30//-60-3.1	30//-60-3	5	157000	54.562
30//-60-3.2	30//-60-3	2.5	199000	82.523

Appendix C

Appendix C: Test Data

In this appendix the data of all the laminates is presented that are not in Chapter 6. The colours and line themselves of the regression curves are the same as the resistance curves that can be found in Chapter 6. This appendix is divided into two sections. First, the resistance curves are shown and in the next and last section the differences between the two cameras are noted.

C.1 da/dN vs G_{max} Plots

In this section the resistance curves of all the layups except the 0//0 specimens are shown.

C.2 Crack Length Difference

In this section the difference in cracklength between the two cameras is calculated and noted in tables. This includes every layup except the ones with a 0°//0° interface.

Table C.1: Differences in crack length of 0°//45° specimens every 50 cycles

Photo	Difference in cracklength (mm)			
#	0//45-1.1	0//45-1.2	0//45-2.1	0//45-2.2
1	-1.274	1.812	0.288	4.249
51	-1.293	1.289	0.22	4.177
101	-0.757	0.937	0.031	5.179
151	-0.323	1.045	-0.17	4.943
201	-0.352	0.842	0.448	5.421
251		0.483		5.028

Figure C.1: da/dN vs Gmax graph of the $0°//45°$ interface.

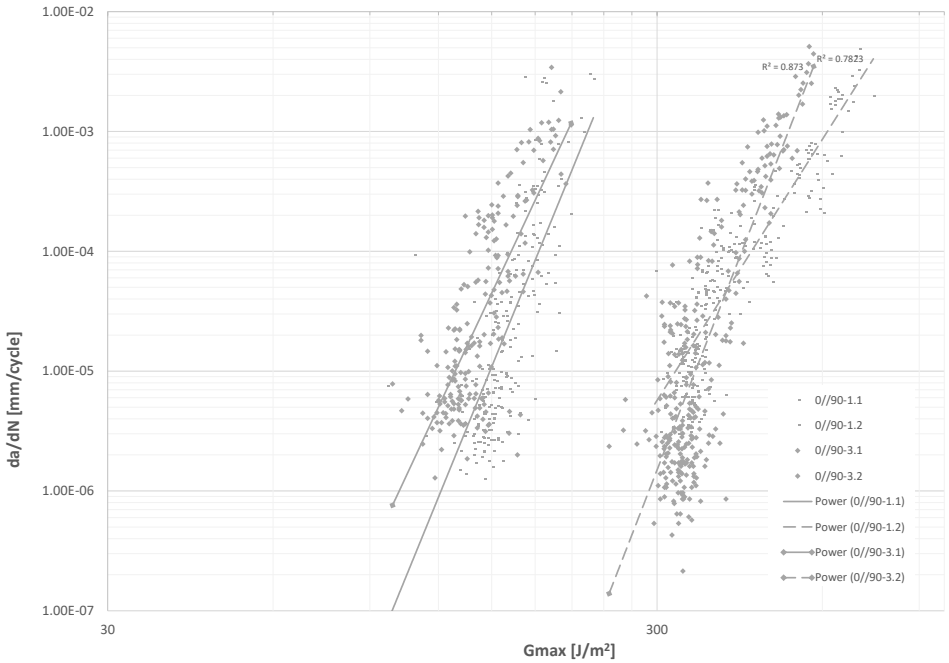

Figure C.2: da/dN vs Gmax graph of the $0°//90°$ interface.

Figure C.3: da/dN vs Gmax graph of the $45°//45°$ interface.

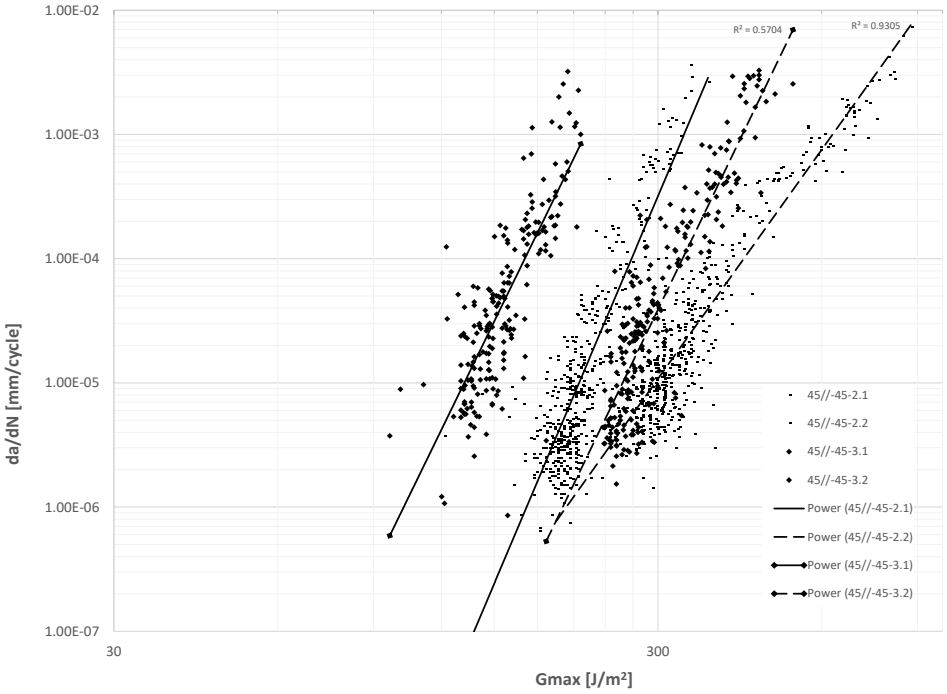

Figure C.4: da/dN vs Gmax graph of the $45°//-45°$ interface.

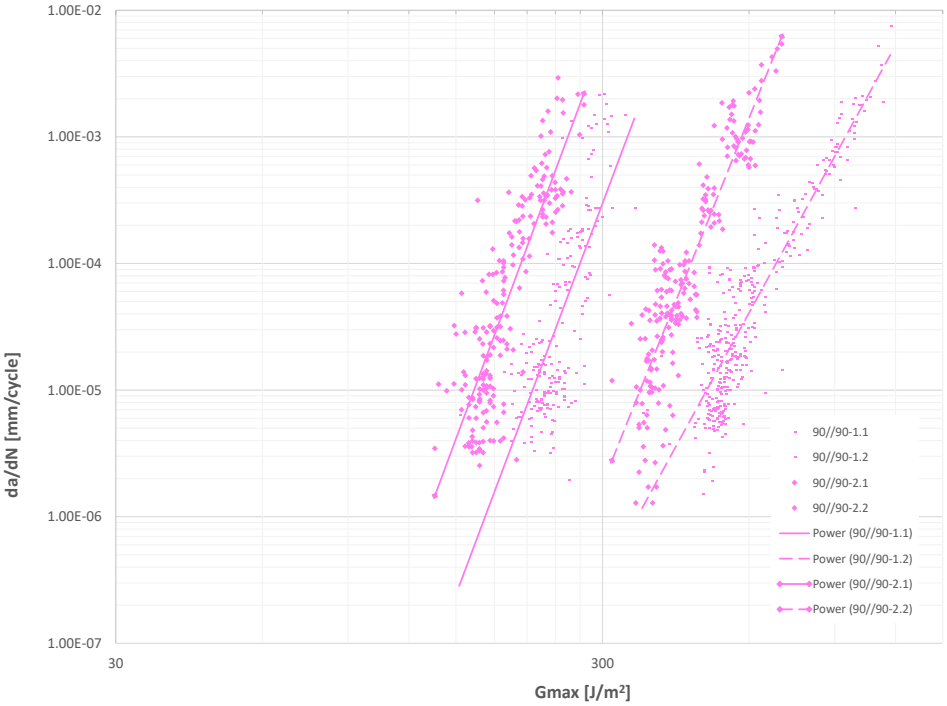

Figure C.5: da/dN vs Gmax graph of the $90°//90°$ interface.

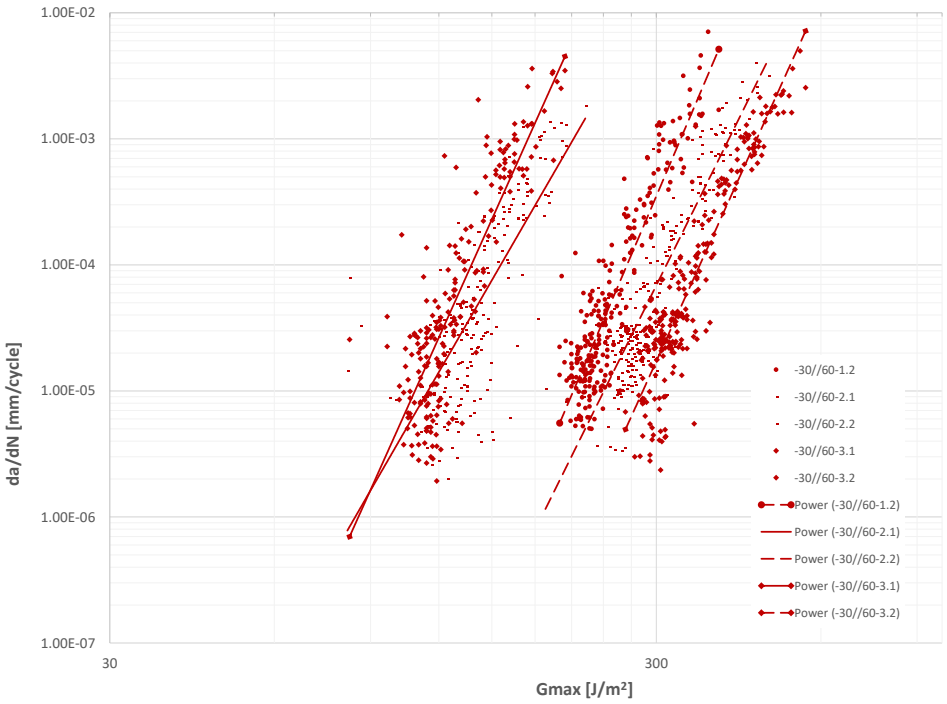

Figure C.6: da/dN vs Gmax graph of the $30°//-60°$ interface.

Table C.2: Differences in crack length of $0°//90°$ specimens every 50 cycles

Photo	Difference in cracklength (mm)			
#	0//90-1.1	0//90-1.2	0//90-2.1	0//90-2.2
1	5.134	2.821	7.103	6.659
51	3.959	4.108	8.094	3.747
101	4.16	5.627	7.999	2.256
151	4.722	4.169	8.702	4.995
201	4.813	4.276	9.224	5.521
251		4.394		5.855
301				5.723

Table C.3: Differences in crack length of $90°//90°$ specimens every 50 cycles

Photo	Difference in cracklength (mm)			
#	90//90-1.1	90//90-1.2	90//90-2.1	90//90-2.2
1	6.625	-0.115	7.009	4.88
51	7.218	0.62	7.327	0.529
101	8.074	4.669	4.617	-2.452
151	8.044	4.881	5.521	-2.941
201	7.888	4.673	5.296	-3.885
251		5.268		
301		4.44		
351		3.785		

Table C.4: Differences in crack length of $45°//-45°$ specimens every 50 cycles

Photo	Difference in cracklength (mm)			
#	45//-45-2.1	45//-45-2.2	45//-45-3.1	45//-45-3.2
1	1.045	2.932	-0.64	1.41
51	1.769	2.074	0.345	-0.081
101	1.755	1.293	1.079	0.49
151	1.469	1.353	0.614	0.357
201	1.208	0.75	0.534	0.7
251	1.793	0.588		1.065
301	2.351	0.872		
351	2.084	1.275		
401	1.995	1.026		
451	2.469	1.352		
501		1.227		

Table C.5: Differences in crack length of $45°//45°$ specimens every 50 cycles

Photo	Difference in cracklength (mm)			
#	45//45-2.1	45//45-2.2	45//45-3.1	45//45-3.2
1	1.396	3.088	1.044	3.453
51	1.008	2.304	1.105	2.203
101	1.625	2.225	1.456	1.595
151	1.489	2	1.904	1.512
201	1.815	2.163		1.063
251	1.898	1.974		0.848
301	2.086	1.605		0.589
351	2.296	1.486		0.9
401	2.387	1.309		1.124
451	2.335			1.302
501				1.073
551				0.964
601				0.936

Table C.6: Differences in crack length of $30°// - 60°$ specimens every 50 cycles

Photo	Difference in cracklength (mm)				
#	30//-60-1.2	30//-60-2.1	30//-60-2.2	30//-60-3.1	30//-60-3.2
1	7.98	7.409	11.065	9.235	8.171
51	8.602	9.676	11.549	8.262	9.955
101	8.035	9.471	10.384	7.502	7.835
151	7.488	8.186	10.713	7.591	7.979
201	7.648	8.476	10.249	7.229	7.554
251	7.517		10.383		7.842

Appendix D

Appendix D: Fractography

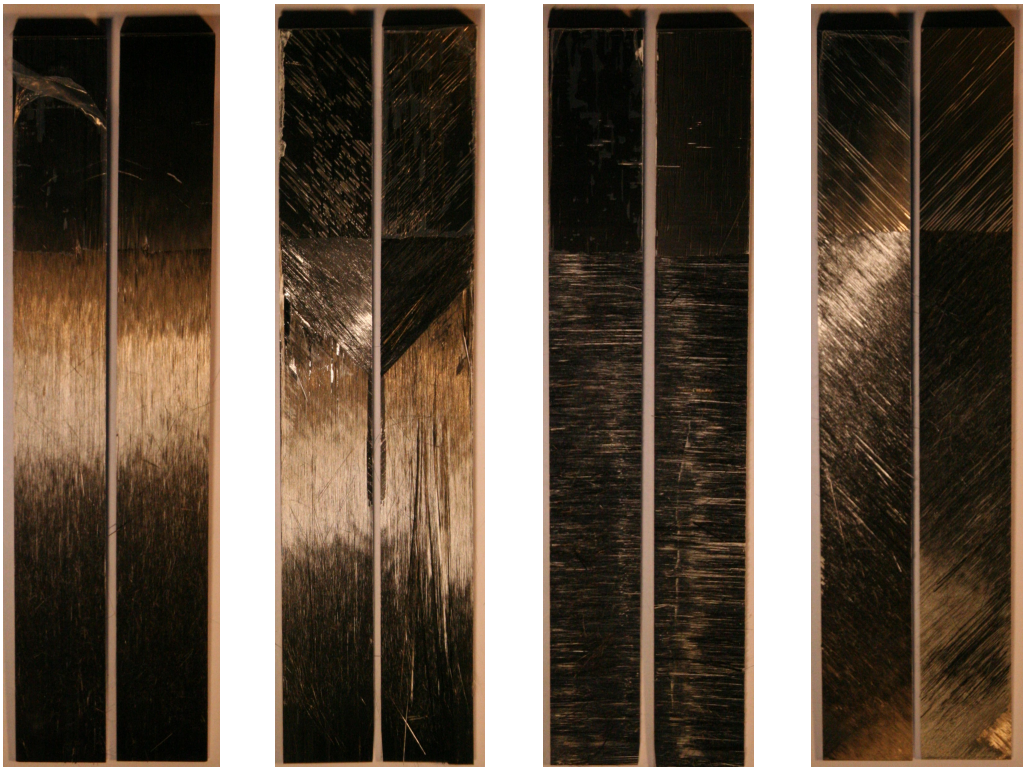

(a) 0//0-2 **(b)** 0//45-1 **(c)** 0//90-3 **(d)** 45//45-2

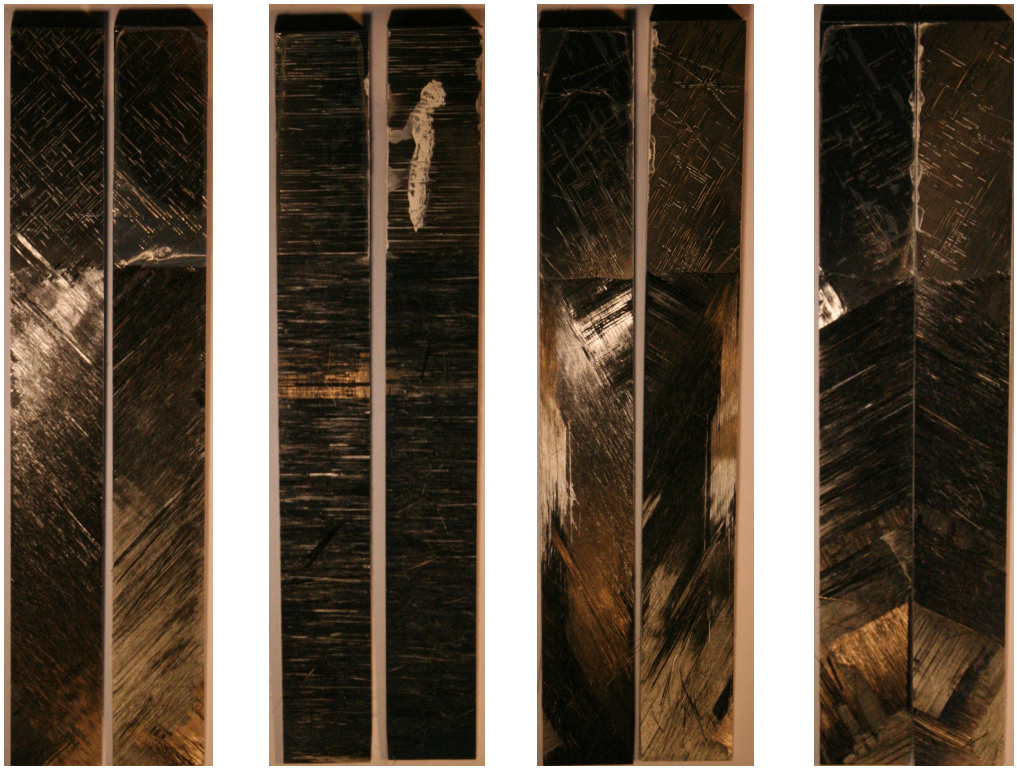

(e) 45//-45-2 **(f)** 90//90-2 **(g)** 30//-60-1 **(h)** 30//-60-3

Figure D.1: Top view of the specimens' interface after the test